

A NEAR-INFRARED SPECTROSCOPIC SURVEY OF K-SELECTED GALAXIES AT  $z \sim 2.3$ : REDSHIFTS AND IMPLICATIONS FOR BROADBAND PHOTOMETRIC STUDIES<sup>1,2</sup>MARISKA KRIEK<sup>3,4,5</sup>, PIETER G. VAN DOKKUM<sup>4</sup>, MARIJN FRANX<sup>3</sup>, GARTH D. ILLINGWORTH<sup>6</sup>, DANILO MARCHESINI<sup>4</sup>, RYAN QUADRI<sup>4,3</sup>, GREGORY RUDNICK<sup>7</sup>, EDWARD N. TAYLOR<sup>3</sup>, NATASCHA M. FÖRSTER SCHREIBER<sup>8</sup>, ERIC GAWISER<sup>4,9</sup>, IVO LABBÉ<sup>10</sup>, PAULINA LIRA<sup>11</sup> AND STIJN WUYTS<sup>3,12</sup>*Accepted for publication in ApJ*

## ABSTRACT

Using the Gemini Near-InfraRed Spectrograph (GNIRS), we have completed a near-infrared spectroscopic survey for  $K$ -bright galaxies at  $z \sim 2.3$ , selected from the MUSYC survey. We derived spectroscopic redshifts from emission lines or from continuum features and shapes for all 36 observed galaxies. The continuum redshifts are driven by the Balmer/4000 Å break, and have an uncertainty in  $\Delta z/(1+z)$  of  $< 0.019$ . We use this unique sample to determine, for the first time, how accurately redshifts and other properties of massive high-redshift galaxies can be determined from broadband photometric data alone. We find that the photometric redshifts of the galaxies in our sample have a systematic error of 0.08 and a random error of 0.13 in  $\Delta z/(1+z)$ . The systematic error can be reduced by using optimal templates and deep photometry; the random error, however, will be hard to reduce below 5%. The spectra lead to significantly improved constraints for stellar population parameters. For most quantities this improvement is about equally driven by the higher spectral resolution and by the much reduced redshift uncertainty. Properties such as the age,  $A_V$ , current star formation rate, and the star formation history are generally very poorly constrained with broadband data alone. Interestingly stellar masses and mass-to-light ratios are among the most stable parameters from broadband data. Nevertheless, photometric studies may overestimate the number of massive galaxies at  $2 < z < 3$ , and thus underestimate the evolution of the stellar mass density. Finally, the spectroscopy supports our previous finding that red galaxies dominate the high-mass end of the galaxy population at  $z = 2 - 3$ .

*Subject headings:* galaxies: high redshift — galaxies: distances and redshifts — galaxies: evolution

## 1. INTRODUCTION

The extensive use of photometric redshifts has greatly enhanced our knowledge of the  $z = 2 - 3$  universe. While color criteria, such as the Lyman break technique (Steidel et al. 1996a,b), distant red galaxy selection (DRGs, Franx et al. 2003; van Dokkum et al. 2003) and BzK selection (Daddi et al.

2004) provide an easy identification of high-redshift galaxies, photometric redshifts allow the study of apparently unbiased samples. Our current understanding of the evolution of the mass-density (e.g., Rudnick et al. 2001, 2003, 2006; Dickinson et al. 2003; Drory et al. 2005) and the luminosity function (e.g., Dahlen et al. 2005; Saracco et al. 2006; Marchesini et al. 2007), the nature of massive high-redshift galaxies (e.g., Förster Schreiber et al. 2004; Labbé et al. 2005; van Dokkum et al. 2006; Papovich et al. 2006), and galaxy clustering (e.g., Daddi et al. 2003; Quadri et al. 2007a; Foucaud et al. 2007) essentially all rely on photometric redshifts.

Ideally, all these studies would have been based on spectroscopic redshifts. However, obtaining spectroscopic redshifts for the required samples is hampered by several obstacles. Due to their faintness, obtaining redshifts of high-redshift galaxies requires long integrations on 8-10m class telescopes. The largest samples of spectroscopically confirmed high redshift galaxies number in the 1000s (e.g., Steidel et al. 2003), several orders of magnitude short of the largest photometric samples. Furthermore, and more fundamentally, current spectroscopic samples are strongly biased towards blue, star forming galaxies which are bright in the observer's optical (Lyman break galaxies, or LBGs). However, it has become clear that the typical massive galaxy at this redshift range is red in the rest-frame optical and faint in the rest-frame ultra-violet (UV), and blue LBGs constitute only  $\sim 20\%$  of massive galaxies at  $z = 2 - 3$  (van Dokkum et al. 2006).

Electronic address: mariska@astro.princeton.edu

<sup>1</sup> Based on observations obtained at the Gemini Observatory, which is operated by the Association of Universities for Research in Astronomy, Inc., under a cooperative agreement with the NSF on behalf of the Gemini partnership.

<sup>2</sup> Fully reduced spectra and corresponding data products will be made public at <http://www.astro.yale.edu/MUSYC> on January 15, 2008

<sup>3</sup> Leiden Observatory, Leiden University, PO Box 9513, 2300 RA Leiden, Netherlands

<sup>4</sup> Department of Astronomy, Yale University, New Haven, CT 06520

<sup>5</sup> *Current address:* Department of Astrophysical Sciences, Princeton University, Princeton, NJ 08544

<sup>6</sup> UCO/Lick Observatory, University of California, Santa Cruz, CA 95064

<sup>7</sup> Goldberg Fellow, National Optical Astronomy Observatory, 950 North Cherry Avenue, Tucson, AZ 85719

<sup>8</sup> Max-Planck-Institut für extraterrestrische Physik, Giessenbachstrasse, Postfach 1312, D-85748 Garching, Germany

<sup>9</sup> Department of Physics and Astronomy, Rutgers University, Piscataway, NJ 08854

<sup>10</sup> Hubble Fellow, Carnegie Observatories, 813 Santa Barbara Street, Pasadena, CA 91101

<sup>11</sup> Departamento de Astronomía, Universidad de Chile, Casilla 36-D, Santiago, Chile

<sup>12</sup> Harvard-Smithsonian Center for Astrophysics, 60 Garden Street, Cambridge, MA 02138

TABLE 1  
SAMPLE AND OBSERVATIONS

ID	RA	DEC	$K_s$	$R$	$J - K$	observation dates	Exptime min	ID <sub>KR06B+07</sub> <sup>a</sup>
1030-32	10 30 41.5	5 19 55	19.68	26.83	2.62	2006/12/19 + 2007/03/12	230	-
1030-101	10 30 10.1	5 20 11	18.97	25.63	2.15	2006/02/23	120	-
1030-301	10 30 50.8	5 20 49	18.82	25.49	2.81	2006/01/20	90	-
1030-609	10 30 49.6	5 21 50	19.68	24.23	2.02	2006/02/24	130	-
1030-807	10 30 20.0	5 22 33	19.72	24.77	2.40	2006/02/23	120	-
1030-1531	10 30 38.9	5 24 52	19.38	22.92	2.23	2006/02/25	80	-
1030-1611	10 30 48.4	5 25 03	19.58	25.55	2.37	2006/02/24	120	-
1030-1813	10 30 51.2	5 25 36	19.01	24.97	2.93	2006/01/20	80	-
1030-1839	10 30 45.4	5 30 07	19.61	24.20	2.35	2006/12/16	80	-
1030-2026	10 30 22.7	5 28 26	19.48	25.22	2.93	2006/02/22	120	-
1030-2329	10 30 16.2	5 27 32	19.72	25.24	2.47	2006/02/25	120	-
1030-2559	10 30 40.1	5 26 34	19.62	25.89	2.52	2006/02/22	110	-
1030-2728 <sup>b</sup>	10 30 18.4	5 26 05	19.52	25.09	2.69	2006/01/21	120	-
1030-2927	10 30 43.3	5 29 34	19.48	24.52	2.23	2006/12/18 + 2007/03/13	230	-
1256-0	12 54 59.6	1 11 30	19.26	24.98	2.26	2005/05/19+27+30 + 2006/02/24	305	151
1256-142	12 55 02.7	1 07 32	19.45	25.99	2.54	2006/02/23	120	465
1256-519	12 55 08.4	1 06 14	18.99	25.51	2.55	2006/02/25	80	-
1256-1207	12 55 19.7	1 12 46	19.25	25.34	2.04	2006/02/25	80	-
1256-1967	12 55 25.8	1 03 25	18.71	23.55	2.02	2005/05/18 + 2006/01/18	240	2889
HDFS1-259	22 33 11.2	-60 40 47	19.42	24.00	2.11	2006/12/17-18	140	-
HDFS1-1849	22 33 37.9	-60 33 15	19.30	25.18	2.51	2004/09/06	115	-
HDFS2-509	22 31 23.1	-60 39 08	18.57	23.20	2.50	2005/05/16+19	235	-
HDFS2-1099	22 32 03.2	-60 36 13	19.26	24.94	2.55	2006/12/19	120	-
HDFS2-2046	22 32 30.8	-60 32 44	19.38	24.24	2.21	2005/05/20	125	-
ECDFS-4454	3 32 11.5	-27 55 23	19.24	24.28	2.89	2006/01/18	100	3662
ECDFS-4511	3 32 43.2	-27 55 15	18.77	23.36	2.62	2006/01/21 + 2006/02/25	190	3694
ECDFS-4713	3 31 52.5	-27 54 48	18.68	22.94	2.13	2006/02/22	60	3896
ECDFS-5856	3 32 13.3	-27 52 26	19.42	25.42	3.21	2006/01/19	120	4937
ECDFS-6842	3 31 51.3	-27 50 56	19.09	24.47	2.47	2006/12/19 + 2007/03/11+14	210	-
ECDFS-6956	3 32 02.5	-27 50 46	19.16	23.40	2.43	2006/01/20 + 2006/02/24	150	5754
ECDFS-9822	3 31 33.9	-27 46 03	19.14	24.13	3.04	2006/12/17	120	-
ECDFS-11490	3 32 45.0	-27 43 09	19.25	24.01	2.49	2006/01/20+21	190	9510
ECDFS-12514	3 31 39.5	-27 41 20	19.11	22.79	1.72	2006/02/23	90	10525
ECDFS-13532	3 31 54.8	-27 39 23	19.52	24.98	3.51	2006/12/18	160	-
ECDFS-16671	3 31 58.9	-27 35 16	18.99	22.08	1.74	2006/12/16	60	-
CDFS-6202	3 32 31.5	-27 46 23	19.04	23.62	2.28	2004/09/02+03	90	6036

<sup>a</sup> ID numbers in Kriek et al. (2006b, 2007)

<sup>b</sup> The spectroscopic redshift of this galaxy has first been confirmed using  $K$ -band spectroscopy with NIRSPEC on Keck, in 2005 January.

Obtaining spectroscopic redshifts for typical massive galaxies requires deep spectroscopy at near-infrared (NIR) wavelengths. Unfortunately, NIR observations are complicated by the combination of the high sky brightness, numerous bright and variable night sky lines and strong atmospheric absorption bands, and the limited field of view of current and planned NIR spectrographs. Thus, obtaining spectroscopic redshifts for hundreds or thousands of galaxies with  $K \sim 21$  (the typical brightness of galaxies with  $M > 10^{11} M_\odot$  at  $z \sim 2.5$ ) will not be feasible in the foreseeable future. Until the next generation of space missions and  $> 20$  m ground-based telescopes we remain largely dependent on photometric redshifts for studies of large and faint galaxy samples beyond  $z > 1.5$ .

Our provisional dependency on broadband photometric studies requires a more accurate calibration and understanding of the involved systematics. The current spectroscopic samples used for calibration of photometric high-redshift studies are based primarily on optical spectroscopy. As these samples are biased towards unobscured star-forming galaxies, their calibration may not be representative for the total sample of massive galaxies. Photometric properties of red, massive galaxies at high redshift are poorly calibrated, and since red galax-

ies dominate the high mass end at  $2 < z < 3$ , systematics may have large effects on the final results.

NIR spectroscopy on a substantial, unbiased sample of massive, high-redshift galaxies is needed to test our photometric studies, and obtain insights regarding possible systematic effects. The Gemini Near-Infrared Spectrograph (GNIRS, Elias et al. 2006) is especially well-suited for spectroscopy of  $z \sim 2.3$  galaxies, due to the large wavelength coverage offered by the cross-disperser (0.9–2.5  $\mu\text{m}$ ). This coverage offers two advantages: there is a large probability of finding emission lines, and it allows the characterization of the continuum emission, which is particularly important for galaxies without detected lines. In Kriek et al. (2006b) we found that a substantial fraction of the massive galaxies at  $z \sim 2.3$  have no detected emission lines. For these galaxies we derived spectroscopic redshifts by modeling the stellar continuum, driven by the Balmer/4000 Å break (Kriek et al. 2006a).

In this paper we present our full survey of  $K$ -selected galaxies at  $z \sim 2.3$ , conducted with GNIRS on Gemini-South between September 2004 and March 2007. In total we integrated more than  $\sim 80$  hours, divided over 6 observing runs, on a sample of 36 galaxies. In previous papers based on preliminary results of this survey

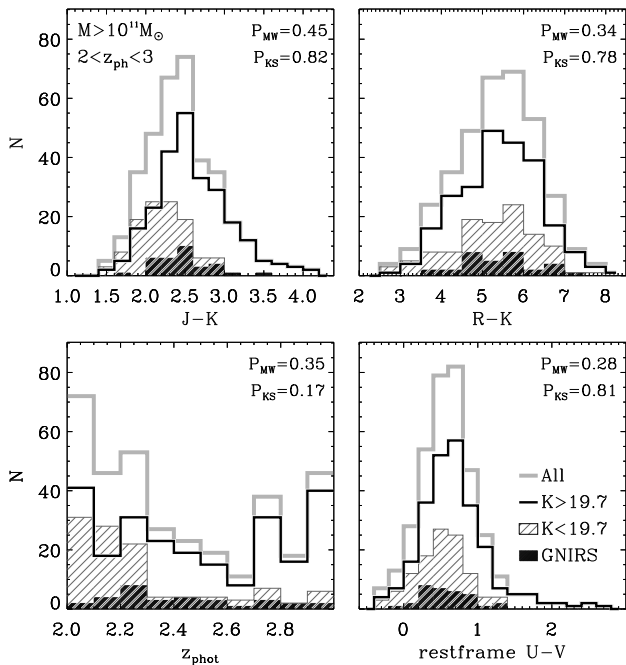


FIG. 1.— Comparison between the photometric properties of the GNIRS sample at  $2 < z_{\text{phot}} < 3$  and a mass-limited sample ( $M > 10^{11} M_{\odot}$ ) at  $2 < z_{\text{phot}} < 3$ . The probabilities ( $P$ ) that the GNIRS sample and the full mass-selected sample have similar distributions, as derived using a Mann-Whitney (MW) and a Kolmogorov-Smirnov (KS) test, are given in the panels. Additionally, we divide the mass-selected sample into its  $K$ -bright ( $K < 19.7$ ) and  $K$ -faint ( $K > 19.7$ ) members. The GNIRS sample may be less representative for a  $K$ -bright sample, as the redshift distribution is different.

we discussed the stellar populations (Kriek et al. 2006b) and the origin of the line emission (Kriek et al. 2007). In this paper we will give an overview of the total survey (§ 2), compare photometric and spectroscopic redshifts (§ 3) and stellar populations properties (§ 4), and discuss the implications for photometric studies (§ 4).

Throughout the paper we assume a  $\Lambda$ CDM cosmology with  $\Omega_m = 0.3$ ,  $\Omega_{\Lambda} = 0.7$ , and  $H_0 = 70 \text{ km s}^{-1} \text{ Mpc}^{-1}$ . The broadband magnitudes are given in the Vega-based photometric system unless stated otherwise. Furthermore, we will measure the scatter and the offset between various properties using the normalized biweight mean absolute deviation and the biweight mean, respectively (Beers, Flynn & Gebhardt 1990). As biweight statistics are less sensitive towards outliers than the normal mean, and more efficient than the median, they are most appropriate for the small sample sizes in this work.

## 2. DATA

### 2.1. Sample Selection

The galaxies studied in this paper are selected from the Multi-wavelength Survey by Yale-Chile (MUSYC, Gawiser et al. 2006; Quadri et al. 2007b). This survey consist of optical imaging (UBVRIZ) of four  $30' \times 30'$  fields, shallow NIR imaging (JHK) over the same area, and deeper NIR imaging over four  $10' \times 10'$  fields. The depth of the deep and wide NIR photometry is  $K \sim 21$  and  $K \sim 20$  ( $5\sigma$ ) respectively. The spectroscopic follow-up presented in this paper is selected from the deep fields HDF-South, 1030, and 1256 (Quadri et al. 2007b), and the shallow extended Chandra Deep Field South (ECDFS, E.N. Taylor et al. 2007, in preparation). One

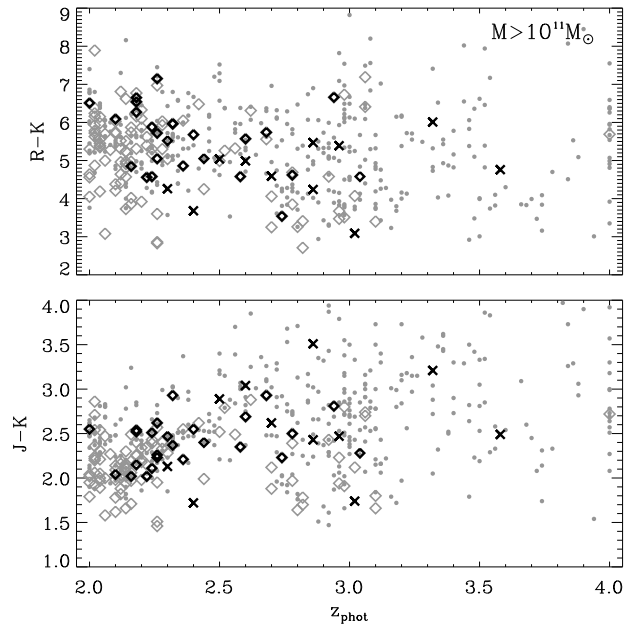


FIG. 2.— Comparison of  $J-K$  and  $R-K$  colors as a function of  $z_{\text{phot}}$  between a photometric mass-limited ( $M > 10^{11} M_{\odot}$ ) sample and our spectroscopic sample. The gray diamonds and dots represent all massive galaxies in the deep MUSYC fields (SDSS1030, 1256 and HDF-S) with  $K < 19.7$  and  $K > 19.7$  respectively. The black symbols represent the 36 galaxies of the GNIRS sample, selected from both the MUSYC deep (diamonds) and wide (ECDFS, crosses) surveys.

galaxy is selected from the Great Observatories Origins Deep Survey (GOODS; Giavalisco et al. 2004). The optical-to-NIR photometry that we used as part of this work is described by S. Wuyts et al. (2007, in preparation).

We selected galaxies with  $2.0 \lesssim z_{\text{phot}} \lesssim 2.7$  (see § 3.2) and  $K \lesssim 19.7$ . This redshift interval is chosen as the bright emission lines  $H\beta$ ,  $[\text{O III}]$ ,  $H\alpha$ , and  $[\text{N II}]$  fall in the  $H$  and  $K$  atmospheric windows. A few galaxies had  $2.7 \lesssim z_{\text{phot}} \lesssim 3.0$  at the time of selection, but were observed because a large part of their confidence intervals fell in the targeted redshift range, or because the galaxy had a known  $z_{\text{spec}}$  between 2.0 and 2.7 (CDFS-6202, van Dokkum et al. 2005; Daddi et al. 2005). Due to catalog updates of the ECDFS field, the final  $z_{\text{phot}}$  of several more galaxies scattered out of the selected redshift range. The fact that the ECDFS catalog was still in a preliminary stage at the time of selection may complicate some of the interpretation in this work. For this reason and the fact that the ECDFS is the only field with shallow NIR photometry, the analysis in this paper will also focus on the subsample excluding the ECDFS.

In total we obtained usable NIR spectra for a sample of 36 galaxies. For  $\sim 4$  additional galaxies we obtained empty spectra due to mis-alignment or extremely bad weather conditions.

It is important to establish whether our sample is representative for the galaxy population at  $z \sim 2.5$ . In Figure 1 we compare the distributions of  $J-K$ ,  $R-K$ , restframe  $U-V$  color and  $z_{\text{phot}}$  of our spectroscopic sample with a photometric mass-limited sample ( $> 10^{11} M_{\odot}$ ) at  $2 < z < 3$ . For the latter we use the deep MUSYC fields, as the wide NIR data are too shallow to extract a mass-limited sample (van Dokkum et al. 2006). Accord-

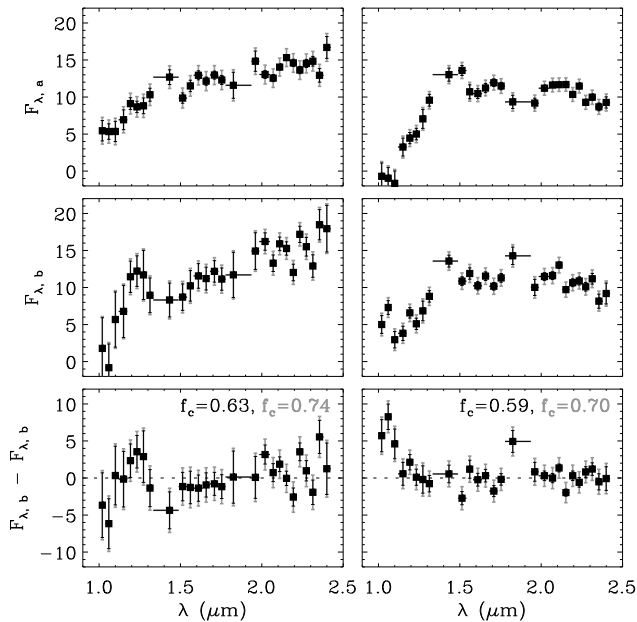


FIG. 3.— The differences between the low resolution spectra of two observing sequences for the same galaxy (left: 1030-301, right: 1256-0) are used to estimate a systematic uncertainty on the spectra. In order to improve the consistency between the different observing sequences, we increase the original uncertainty per bin (black error bars) by a systematic error of 10% (gray error bars) of the average flux in the binned spectrum. The fractions of bins that are consistent within  $1\sigma$  for the original and increased uncertainties are given in the panels in black and gray respectively.

ing to a Mann-Whitney and a Kolmorov-Smirnov test, the photometric properties  $J - K$ ,  $R - K$ , rest-frame  $U - V$  color (as derived from the photometry) and  $z_{\text{phot}}$  of the GNIRS sample are representative for a photometric mass-limited sample at  $2 < z < 3$  (see probabilities in panels of Fig. 1). The Mann-Whitney test assesses whether the two sample populations are consistent with the same mean of distribution, while the K-S test examines whether the two samples could have been drawn from the same parent distribution. For both tests the probability should be greater than the 0.05 significance level.

The galaxies targeted with GNIRS are all bright in  $K$  ( $< 19.7$ ). In order to examine if bright galaxies are a biased sub-sample of the total mass-limited sample, we split the sample in bright and faint members. Figure 1 shows that the bright and faint members have the same distribution of rest-frame  $U - V$  and observed  $R - K$  colors. The main difference between the bright and faint members is the redshift distribution: almost all  $K$ -bright galaxies have  $z_{\text{phot}} < 2.3$ . This also causes their bluer  $J - K$  colors: in contrast to the  $R$ -band, the  $J$ -band does not fall entirely bluewards of the optical break for  $z < 2.3$ . The redshift dependence of  $J - K$  is clearly visible in Figure 2. However, except for the difference in redshift and presumably stellar mass, we see no hints that the bright and faint members of a mass-limited sample at  $2 < z < 3$  have different stellar populations. Thus, although the spectroscopic sample may have similar stellar population properties as  $K$ -bright galaxies, it is less representative for a  $K$ -bright sample at  $2 < z < 3$ , as the median redshift and its corresponding distribution is substantially different.

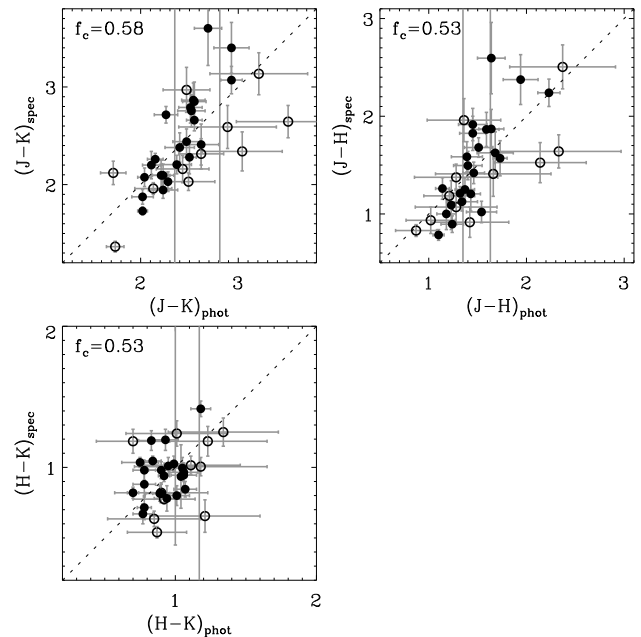


FIG. 4.— Comparison of photometric NIR colors, and those derived from the spectra, for galaxies in the deep (solid) and wide (open) MUSYC fields. Both colors are not corrected for flux contributions by emission lines. For a few galaxies the spectra are too noisy to measure the spectroscopic NIR colors. The fraction of galaxies for which the photometric and spectroscopic colors are consistent within  $1\sigma$  is given in the top left corner. As these factors are less than 0.68, the errors may be slightly underestimated.

## 2.2. NIR spectra

We observed the full sample of 36 galaxies with GNIRS in cross-dispersed mode, in combination with the 32 lines  $\text{mm}^{-1}$  grating and the  $0''.675$  slit. This configuration resulted in a spectral resolution of  $R \sim 1000$ . The galaxies were observed during six observing runs in 2004 September (program GS-2004B-Q-38), 2005 May (program GS-2005A-Q-20), 2006 January (program GS-2005B-C-12) and 2006 February (program GS-2006A-C-6), 2006 December (program GS-2006B-C-5) and 2007 March (program GS-2007A-C-9). During the first two runs most time was lost due to bad weather, and only a handful of galaxies was observed under mediocre weather condition (seeing  $\sim 1''$ ). The weather was excellent throughout the full 3rd and 4th run, and we reached a median seeing of  $\sim 0''.5$ . The conditions were slightly worse during the last two runs, with a median seeing of  $\sim 0''.7$ , and some time was lost due to clouds.

We observed the galaxies following an ABA'B' on-source dither pattern, such that we can use the average of the previous and following exposures as sky frame. This cancels sky variation and reduces the noise in the final frame. All targets were acquired by blind offsets from nearby stars. The individual exposures are 5 minutes for the galaxies observed during the first two runs, and 10 minutes for the remaining runs<sup>13</sup>. The total integration times for all galaxies are listed in Table 1. Before and after every observing sequence we observe an A V0 star, for the purpose of correcting for telluric absorption. The

<sup>13</sup> An instrument upgrade after the first two runs improved the throughput and thus the quality of the spectra, and eliminated “radiation events” caused by radioactive coatings. This allowed longer integrations

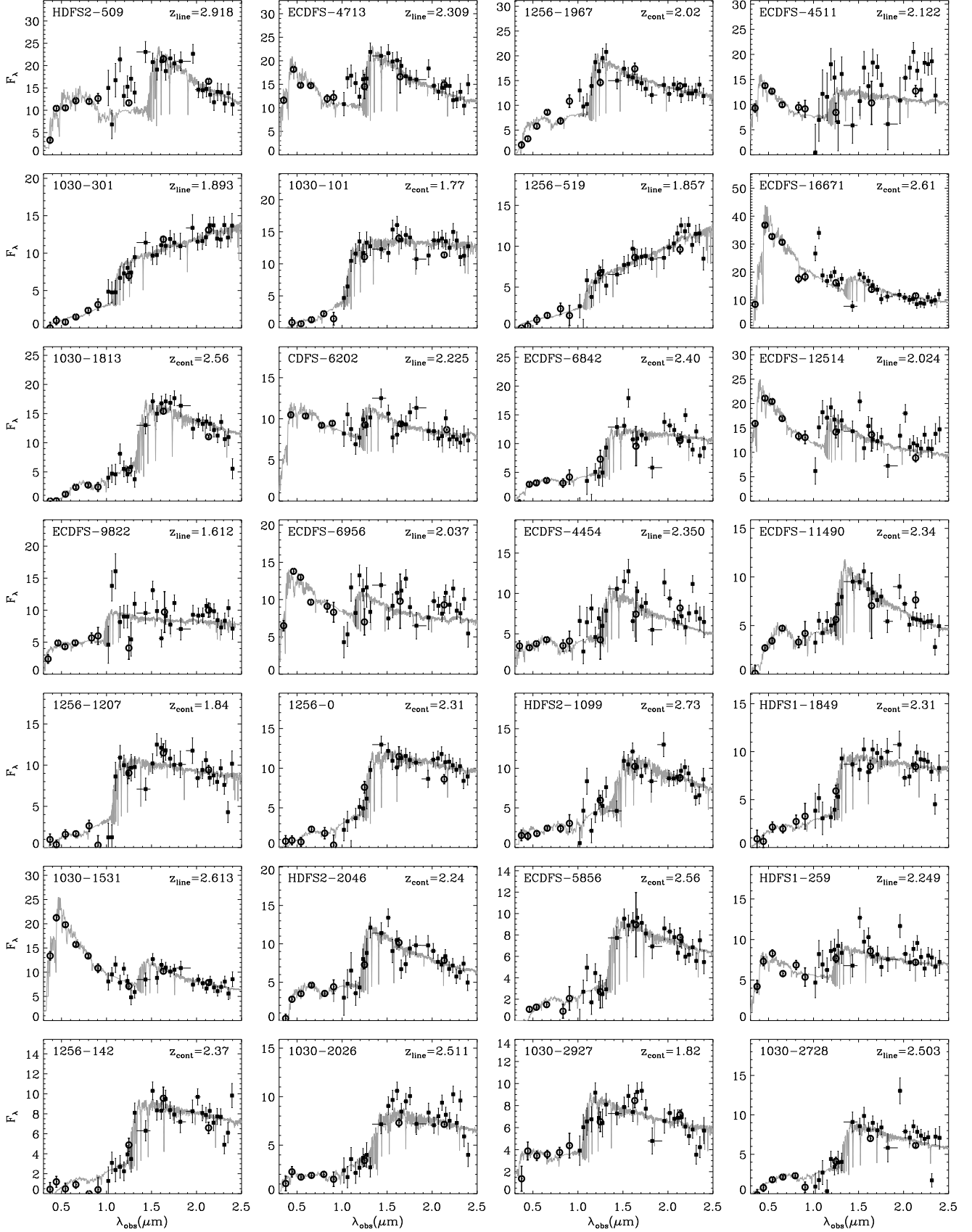
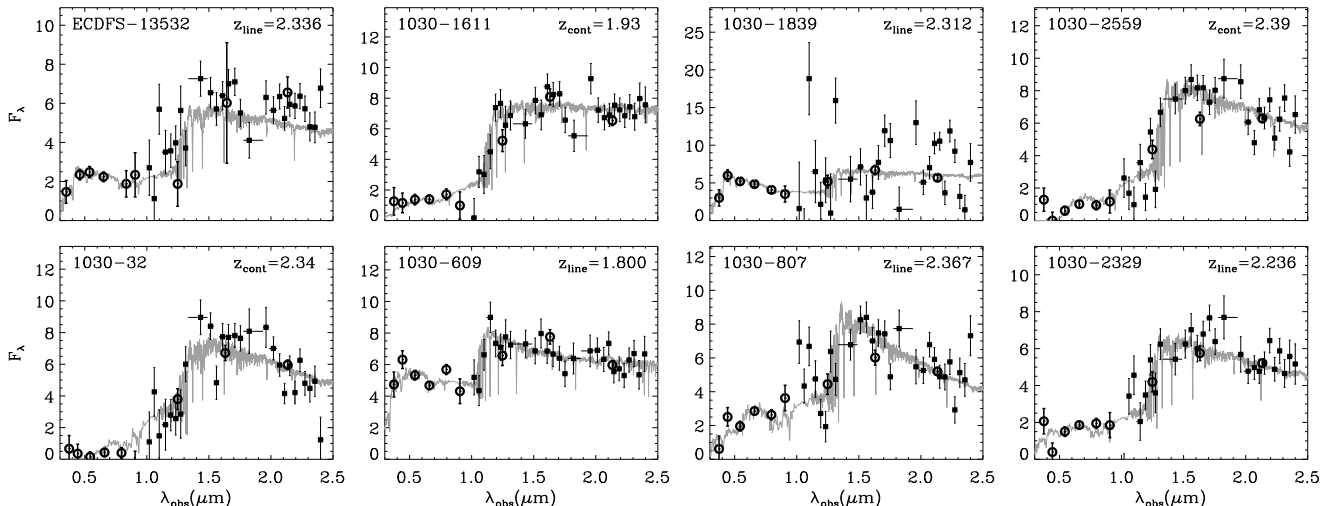


FIG. 5.— GNIRS spectra (*black squares*) and MUSYC broadband photometry (*open circles*) for all 36 galaxies, sorted for their total  $K$ -band magnitude starting with the brightest galaxy (see Table 1). Fluxes are given in  $10^{-19} \text{ ergs s}^{-1} \text{ cm}^{-2} \text{ Å}^{-1}$ . Emission line fluxes are removed from the binned spectra, using the best-fit models to the lines. The photometry is not corrected for emission line contamination. The best-fit stellar population models to the spectra and photometry are shown in gray. For emission-line galaxies the redshift was fixed at  $z_{\text{line}}$  during fitting, while for the remaining galaxies  $z$  was a free parameter.

FIG. 5.— *Continued*

final spectra of the two stars were combined to match the target’s airmass.

A detailed description of the reduction procedure of the GNIRS cross-dispersed spectra is given in Kriek et al. (2006a). In summary, we subtract the sky, mask cosmic rays and bad pixels, straighten the spectra, combine the individual exposures, stitch the orders and finally correct for the response function. 1D spectra are extracted by summing all adjacent lines (along the spatial direction) with a mean flux greater than 0.25 times the flux in the central row, using optimal weighting. We also constructed “low resolution” binned spectra from the 2D spectra for each galaxy following the method as described in Kriek et al. (2006a). Each bin contains 80 “good” pixels (i.e., wavelength regions with high atmospheric transmission and low sky emission), corresponding to 400 Å per bin. Sky, transmission, and noise spectra were constructed for each galaxy as well.

We assess the uncertainties on the low resolution spectra by splitting the data in two sequences for several objects and comparing the results. We find that the errors as derived from the photon noise underestimate the true uncertainty for most galaxies. In Figure 3 we show two examples. In order to obtain a better consistency between the observing sequences, we increase the uncertainties for all bins by quadratically adding 10% of the average flux in the spectrum.

We use the broadband NIR photometry to perform the absolute flux calibration. For each galaxy we integrate the spectrum over the same  $J$ ,  $H$  and  $K$  filter curves as the photometry. We determine one scaling factor per galaxy, from the difference between the spectroscopic and photometric NIR magnitudes, and use this factor to scale the NIR spectrum. We note that at this stage both the spectra and the photometry may contain flux contributions by emission lines. We extend our wavelength coverage by attaching the optical photometry to the scaled spectra. For the emission-line galaxies we subsequently remove the line fluxes from the affected bins, using the best-fit to the emission lines as derived in Kriek et al. (2007).

As a quality check we compare the photometric NIR colors  $J-H$ ,  $J-K$  and  $H-K$  to those derived from the

spectra. The direct comparison for the individual galaxies is presented in Figure 4. As expected, the scatter is larger for the galaxies with shallow NIR photometry. The fraction of galaxies for which the spectroscopic and photometric colors are consistent within  $1\sigma$  are listed in the panels. For all colors these fractions are slightly lower than expected, suggesting that the uncertainties may be slightly underestimated. This may be partly due to color gradients in the galaxies, as we use different apertures to determine the colors. The spectroscopic apertures are rectangular, and depend on the extraction radius and method, which differs per galaxy. On average the spectroscopic apertures are  $0''.675$  by  $1''.2$ , slightly smaller than the circular photometric apertures which have a diameter of  $\sim 1''.4$ .

The final low resolution spectra and broadband photometry for the full sample are presented in Figure 5. The galaxies are ordered by total  $K$  magnitude (see Table 1), starting with the brightest galaxy. Remarkably, there is not a strong trend between quality of the spectrum and the total  $K$ -band magnitude for the same integration time. We suspect that the surface brightness of the object plays an important role, as bright objects with low quality spectra and typical integration times, such as ECDFS-4511 and ECDFS-9822, are extended even in the MUSYC imaging, which have a image quality of  $\sim 1''$ .

### 3. SPECTROSCOPIC VERSUS PHOTOMETRIC REDSHIFTS

#### 3.1. Spectroscopic Redshifts and Galaxy Properties

For 19 of the galaxies in the sample we detected one or more emission lines, and thus for these galaxies we could determine exact spectroscopic redshifts. The remaining galaxies may have no or very faint emission lines, or the lines are expected in atmospheric wavelength regions with low transmission or strong sky emission. Fortunately, we can derive fairly precise redshifts from the continuum emission alone, mainly due to the presence of the Balmer/4000 Å break in the NIR spectra (Kriek et al. 2006a). For none of the galaxies absorption lines are detected.

We fit the low resolution binned spectra together with the optical photometry by Bruzual & Charlot (2003) stellar population models. We allow a grid of 24 different

ages (not allowing the galaxy to be older than the age of the universe), and 31 different exponentially declining star formation histories (SFHs) with the characteristic timescale ( $\tau$ ) varying between 10 Myr and 10 Gyr. We leave redshift as a free parameter for the galaxies without emission lines. Furthermore, we adopt the Calzetti et al. (2000) reddening law and allow 41 values for  $A_V$  between 0 and 4 mag. We compute the  $\chi^2$  surface as function of all stellar population parameters. For all grid points we assume the Salpeter (1955) IMF, and solar metallicity. A Chabrier (2003) or a Kroupa (2001) IMF yield stellar masses and SFRs which are a factor of  $\sim 2$  lower. The mass differences when using the stellar population library by Maraston (2005) are discussed in Kannappan & Gawiser (2007) and Wuyts et al. (2007).

We derive  $1\sigma$  confidence intervals on the redshifts and stellar population properties using 200 Monte Carlo simulations. We vary all bins of the low-resolution spectra according to their uncertainties, and fit the simulated spectra using the same procedure as described above. Next, we determine the contour in the original  $\chi^2$  surface that encompasses 68% of the Monte Carlo simulations (see Papovich et al. 2003; Kriek et al. 2006a). The  $1\sigma$  confidence intervals for all properties are the minimum and maximum values that are allowed within this  $\chi^2$  contour.

For the emission-line galaxies, we removed the emission line fluxes from the spectra before fitting. This is different to our previous method presented in Kriek et al. (2006a) in which we mask the bins that are contaminated by emission lines. The difference in modeling results (although consistent within the errors) compared to Kriek et al. (2006b, 2007) are due to this improvement and updates of the broadband photometry catalogs. All spectroscopic redshifts and corresponding stellar population properties are listed in Table 2.

In order to test the accuracy of the continuum redshifts, we also fit the emission-line galaxies with redshift as a free parameter. In Figure 6 we compare the emission line redshifts with the continuum redshifts. We find a scatter of  $\Delta z/(1+z) = 0.019$  and no significant systematic offset. In Figure 7 we examine causes of the errors. First, as the modeling is driven by the optical break, we expect this method to be less accurate if the break falls between atmospheric windows. In the Figure 7a we indeed find that galaxies for which the break falls outside the spectrum or in between the  $J$  and  $H$  band have less accurate  $z_{\text{cont}}$ .

Furthermore, we expect the continuum redshifts to be more accurate for galaxies with strong optical breaks. In the Figures 7b and c we show the correlation with rest-frame  $U - V$  color and observed  $R - K$  color. If we exclude the galaxies for which the break falls between atmospheric windows (gray symbols), we indeed find that blue galaxies with weak optical breaks, have less accurate continuum redshifts. The continuum redshifts for galaxies without emission lines might even be more accurate, as these galaxies generally have larger breaks (Kriek et al. 2006b).

Finally, in Figure 7d we examine the correlation between  $(z_{\text{cont}} - z_{\text{line}})/(z_{\text{line}} + 1)$  and the S/N per bin. Remarkably, we do not find an obvious trend. However, the different causes for errors and the small size of the

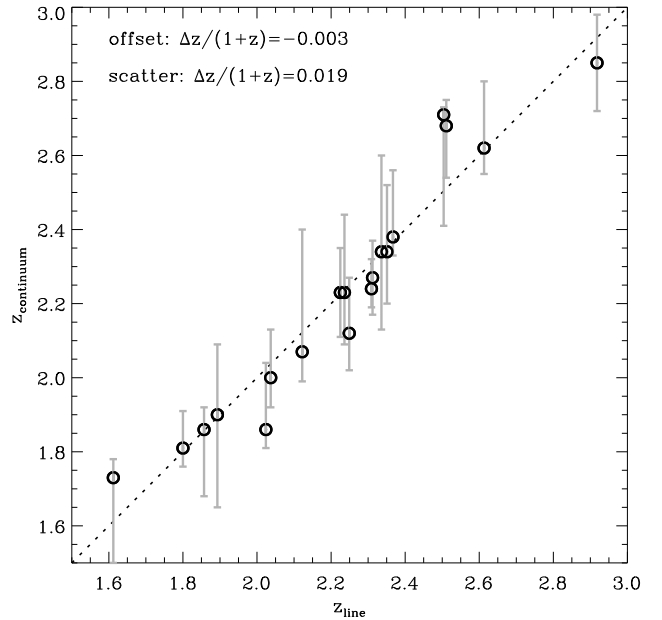


FIG. 6.— In this figure we illustrate the accuracy of continuum redshifts, by deriving  $z_{\text{cont}}$  for the 19 emission-line galaxies in the sample. The scatter and the systematic offset in  $\Delta z/(1+z)$  are listed in the figure. The continuum redshifts are  $\sim 4-7$  times more accurate than photometric redshifts, and show no significant systematic offset. Galaxies without emission lines generally have larger breaks, so their  $z_{\text{cont}}$  may even be more accurate.

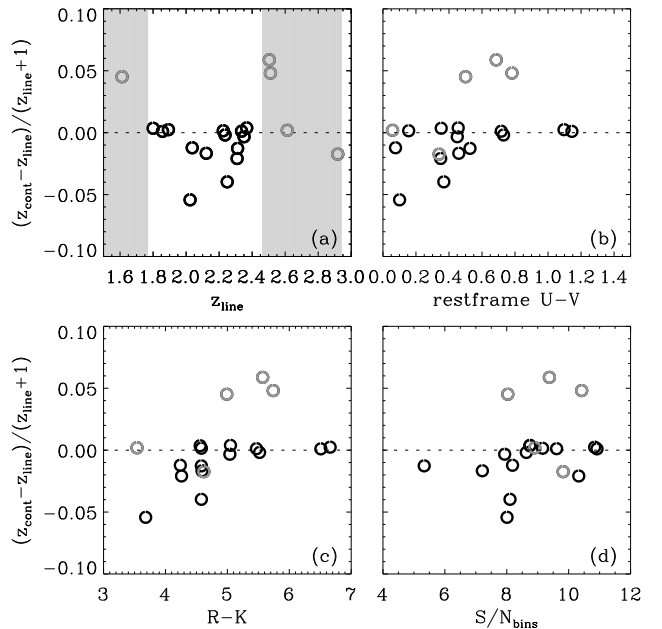


FIG. 7.— In this diagram we examine the cause of errors in continuum redshifts. As the modeling is mainly driven by the optical break, we expect and indeed find less accurate continuum redshifts for galaxies for which a large part of the break falls between atmospheric windows or outside the spectrum (panel a, shaded regions). These galaxies are indicated by gray symbols in all panels. In panels b and c we show that for galaxies with bluer SEDs, and thus weaker optical breaks, the continuum redshifts are less accurate. There is no clear correlation with the S/N of the spectrum in panel d.

sample may have affected a possible correlation.

TABLE 2  
SPECTROSCOPIC MODELING RESULTS

ID	$z^a$	age Gyr	$\tau$ Gyr	$A_V$ mag	$M$ $10^{11} M_\odot$	SFR $M_\odot \text{yr}^{-1}$	$M/L_V$ ( $M/L_V$ ) $_\odot$	V	U-V
1030-32	$2.34^{+0.02}_{-0.12}$	$1.01^{+0.12}_{-0.21}$	$0.040^{+0.080}_{-0.030}$	$0.0^{+0.4}_{-0.0}$	$1.40^{+0.38}_{-0.19}$	$0.0^{+0.1}_{-0.0}$	$0.85^{+0.28}_{-0.07}$	$-23.29^{+0.17}_{-0.03}$	$0.70^{+0.11}_{-0.07}$
1030-101	$1.77^{+0.09}_{-0.11}$	$0.57^{+0.71}_{-0.17}$	$0.020^{+0.130}_{-0.010}$	$1.5^{+0.5}_{-0.8}$	$3.16^{+0.75}_{-1.14}$	$0.0^{+4.4}_{-0.0}$	$2.42^{+0.63}_{-0.54}$	$-23.03^{+0.14}_{-0.28}$	$1.18^{+0.10}_{-0.11}$
1030-301	1.893	$0.20^{+0.60}_{-0.10}$	$0.040^{+0.210}_{-0.030}$	$2.8^{+0.2}_{-0.5}$	$4.48^{+1.24}_{-0.93}$	$87.0^{+294.8}_{-85.3}$	$3.25^{+0.85}_{-0.60}$	$-23.10^{+0.05}_{-0.03}$	$1.10^{+0.14}_{-0.06}$
1030-609	1.800	$0.20^{+0.52}_{-0.10}$	$0.120^{+9.880}_{-0.095}$	$1.8^{+0.2}_{-0.2}$	$0.70^{+0.29}_{-0.17}$	$159.8^{+147.9}_{-111.1}$	$0.91^{+0.35}_{-0.20}$	$-22.46^{+0.05}_{-0.02}$	$0.35^{+0.07}_{-0.05}$
1030-807	2.367	$0.72^{+0.09}_{-0.52}$	$0.100^{+0.020}_{-0.085}$	$0.0^{+1.4}_{-0.0}$	$0.97^{+0.55}_{-0.01}$	$1.0^{+6.3}_{-0.9}$	$0.59^{+0.37}_{-0.00}$	$-23.29^{+0.04}_{-0.01}$	$0.46^{+0.11}_{-0.01}$
1030-1531	2.613	$0.57^{+0.57}_{-0.17}$	$0.650^{+9.350}_{-0.350}$	$0.8^{+0.1}_{-0.1}$	$1.67^{+0.62}_{-0.19}$	$227.1^{+72.7}_{-56.3}$	$0.56^{+0.18}_{-0.06}$	$-23.92^{+0.04}_{-0.05}$	$0.06^{+0.07}_{-0.02}$
1030-1611	$1.93^{+0.14}_{-0.14}$	$0.57^{+1.04}_{-0.37}$	$0.120^{+0.180}_{-0.110}$	$1.7^{+0.6}_{-1.1}$	$2.25^{+0.52}_{-0.67}$	$20.7^{+68.6}_{-20.7}$	$1.97^{+0.98}_{-0.41}$	$-22.85^{+0.36}_{-0.12}$	$0.96^{+0.15}_{-0.12}$
1030-1813	$2.56^{+0.14}_{-0.02}$	$0.51^{+0.21}_{-0.00}$	$0.020^{+0.060}_{-0.010}$	$0.8^{+0.1}_{-0.5}$	$5.04^{+0.93}_{-1.25}$	$0.0^{+1.7}_{-0.0}$	$0.96^{+0.20}_{-0.15}$	$-24.42^{+0.03}_{-0.13}$	$0.72^{+0.07}_{-0.09}$
1030-1839	2.312	$2.00^{+0.75}_{-1.49}$	$4.000^{+6.000}_{-3.800}$	$1.3^{+0.3}_{-0.4}$	$2.83^{+0.94}_{-1.23}$	$143.2^{+129.0}_{-89.7}$	$1.83^{+0.49}_{-0.82}$	$-23.22^{+0.07}_{-0.08}$	$0.53^{+0.09}_{-0.11}$
1030-2026	2.511	$1.14^{+0.29}_{-0.57}$	$0.200^{+0.050}_{-0.080}$	$0.4^{+0.9}_{-0.1}$	$2.68^{+1.45}_{-0.09}$	$6.0^{+27.2}_{-0.7}$	$1.11^{+0.59}_{-0.04}$	$-23.71^{+0.01}_{-0.01}$	$0.78^{+0.10}_{-0.05}$
1030-2329	2.236	$0.81^{+0.33}_{-0.60}$	$0.150^{+0.050}_{-0.140}$	$0.7^{+1.2}_{-0.4}$	$1.44^{+0.41}_{-0.32}$	$5.8^{+34.9}_{-5.8}$	$1.15^{+0.37}_{-0.26}$	$-23.00^{+0.05}_{-0.02}$	$0.73^{+0.06}_{-0.10}$
1030-2559	$2.39^{+0.05}_{-0.16}$	$0.57^{+1.04}_{-0.17}$	$0.010^{+0.190}_{-0.000}$	$0.7^{+0.5}_{-0.7}$	$2.10^{+0.68}_{-0.67}$	$0.0^{+2.5}_{-0.0}$	$1.07^{+0.62}_{-0.23}$	$-23.32^{+0.12}_{-0.20}$	$0.83^{+0.15}_{-0.11}$
1030-2728	2.504	$0.51^{+0.06}_{-0.22}$	$0.080^{+0.020}_{-0.070}$	$0.9^{+0.4}_{-0.3}$	$2.34^{+0.28}_{-0.42}$	$6.4^{+4.0}_{-6.4}$	$1.04^{+0.12}_{-0.18}$	$-23.63^{+0.02}_{-0.02}$	$0.69^{+0.05}_{-0.06}$
1030-2927	$1.82^{+0.20}_{-0.16}$	$0.51^{+0.77}_{-0.41}$	$0.150^{+0.150}_{-0.140}$	$1.3^{+0.5}_{-1.3}$	$1.08^{+0.31}_{-0.38}$	$31.7^{+50.1}_{-31.7}$	$1.23^{+0.35}_{-0.46}$	$-22.61^{+0.30}_{-0.32}$	$0.63^{+0.12}_{-0.15}$
1256-0	$2.31^{+0.05}_{-0.07}$	$0.57^{+0.44}_{-0.28}$	$0.080^{+0.070}_{-0.070}$	$1.2^{+0.6}_{-0.6}$	$4.06^{+1.07}_{-0.78}$	$5.2^{+34.2}_{-5.2}$	$1.51^{+0.46}_{-0.27}$	$-23.82^{+0.11}_{-0.08}$	$0.90^{+0.10}_{-0.08}$
1256-142	$2.37^{+0.05}_{-0.15}$	$0.40^{+2.35}_{-0.12}$	$0.010^{+0.390}_{-0.000}$	$1.3^{+0.4}_{-1.3}$	$3.22^{+1.00}_{-1.08}$	$0.0^{+16.1}_{-0.0}$	$1.46^{+0.76}_{-0.48}$	$-23.60^{+0.21}_{-0.07}$	$0.89^{+0.15}_{-0.11}$
1256-519	1.857	$0.40^{+2.60}_{-0.30}$	$0.250^{+9.750}_{-0.240}$	$3.1^{+0.3}_{-1.0}$	$4.27^{+3.48}_{-1.63}$	$523.4^{+817.5}_{-521.9}$	$4.32^{+3.63}_{-1.60}$	$-22.74^{+0.05}_{-0.04}$	$1.14^{+0.19}_{-0.16}$
1256-1207	$1.84^{+0.05}_{-0.04}$	$0.40^{+0.74}_{-0.12}$	$0.025^{+0.125}_{-0.015}$	$1.5^{+0.3}_{-1.0}$	$2.06^{+0.34}_{-0.52}$	$0.0^{+9.8}_{-0.0}$	$1.70^{+0.29}_{-0.41}$	$-22.96^{+0.09}_{-0.11}$	$0.96^{+0.08}_{-0.08}$
1256-1967	$2.02^{+0.07}_{-0.09}$	$0.20^{+0.00}_{-0.10}$	$0.025^{+0.015}_{-0.015}$	$1.4^{+0.4}_{-0.1}$	$2.48^{+0.40}_{-0.33}$	$3.7^{+48.1}_{-3.7}$	$0.99^{+0.09}_{-0.07}$	$-23.75^{+0.16}_{-0.12}$	$0.53^{+0.05}_{-0.03}$
HDFS1-259	2.249	$0.81^{+0.63}_{-0.52}$	$5.000^{+5.000}_{-4.800}$	$1.5^{+0.2}_{-0.2}$	$2.00^{+0.48}_{-0.60}$	$287.1^{+166.4}_{-108.3}$	$1.14^{+0.27}_{-0.32}$	$-23.36^{+0.04}_{-0.03}$	$0.37^{+0.08}_{-0.10}$
HDFS1-1849	$2.31^{+0.09}_{-0.08}$	$0.40^{+0.74}_{-0.20}$	$0.080^{+0.120}_{-0.070}$	$1.6^{+0.5}_{-1.0}$	$3.47^{+1.00}_{-0.86}$	$35.0^{+91.4}_{-35.0}$	$1.59^{+0.60}_{-0.47}$	$-23.59^{+0.13}_{-0.13}$	$0.84^{+0.11}_{-0.16}$
HDFS2-509	2.918	$0.57^{+0.00}_{-0.00}$	$0.100^{+0.000}_{-0.000}$	$0.0^{+0.1}_{-0.0}$	$3.54^{+0.70}_{-0.00}$	$15.0^{+3.0}_{-0.0}$	$0.52^{+0.00}_{-0.04}$	$-25.02^{+0.10}_{-0.00}$	$0.34^{+0.00}_{-0.05}$
HDFS2-1099	$2.73^{+0.08}_{-0.17}$	$1.01^{+0.00}_{-0.30}$	$0.150^{+0.000}_{-0.050}$	$0.0^{+0.4}_{-0.0}$	$2.83^{+0.89}_{-0.44}$	$2.8^{+4.9}_{-1.5}$	$0.76^{+0.22}_{-0.05}$	$-24.18^{+0.18}_{-0.10}$	$0.59^{+0.10}_{-0.03}$
HDFS2-2046	$2.24^{+0.09}_{-0.04}$	$0.29^{+0.28}_{-0.08}$	$0.012^{+0.068}_{-0.002}$	$0.8^{+0.5}_{-0.6}$	$1.41^{+0.50}_{-0.25}$	$0.0^{+6.5}_{-0.0}$	$0.71^{+0.21}_{-0.11}$	$-23.49^{+0.07}_{-0.14}$	$0.51^{+0.04}_{-0.07}$
ECDFS-4454	2.351	$0.72^{+0.09}_{-0.31}$	$0.120^{+0.030}_{-0.020}$	$0.1^{+1.2}_{-0.1}$	$1.20^{+0.92}_{-0.16}$	$3.2^{+69.7}_{-0.4}$	$0.62^{+0.50}_{-0.05}$	$-23.46^{+0.06}_{-0.03}$	$0.45^{+0.14}_{-0.05}$
ECDFS-4511	2.122	$2.75^{+0.25}_{-0.55}$	$10.000^{+0.000}_{-7.000}$	$1.1^{+0.0}_{-0.1}$	$3.95^{+0.48}_{-0.47}$	$165.9^{+1.5}_{-34.9}$	$1.80^{+0.17}_{-0.20}$	$-23.60^{+0.02}_{-0.03}$	$0.46^{+0.04}_{-0.02}$
ECDFS-4713	2.309	$0.51^{+0.21}_{-0.00}$	$0.150^{+0.150}_{-0.030}$	$0.7^{+0.3}_{-0.2}$	$2.73^{+0.93}_{-0.14}$	$80.0^{+112.0}_{-40.1}$	$0.71^{+0.23}_{-0.07}$	$-24.21^{+0.02}_{-0.05}$	$0.35^{+0.06}_{-0.00}$
ECDFS-5856	$2.56^{+0.12}_{-0.04}$	$0.40^{+0.50}_{-0.12}$	$0.030^{+0.090}_{-0.020}$	$1.0^{+0.4}_{-0.8}$	$2.74^{+0.77}_{-0.68}$	$0.0^{+9.6}_{-0.0}$	$1.06^{+0.31}_{-0.26}$	$-23.78^{+0.06}_{-0.13}$	$0.73^{+0.09}_{-0.11}$
ECDFS-6842	$2.40^{+0.08}_{-0.10}$	$0.57^{+0.24}_{-0.28}$	$0.150^{+0.050}_{-0.100}$	$1.5^{+0.3}_{-0.5}$	$5.35^{+0.90}_{-1.47}$	$103.1^{+137.7}_{-72.4}$	$1.66^{+0.31}_{-0.45}$	$-24.02^{+0.15}_{-0.11}$	$0.81^{+0.06}_{-0.13}$
ECDFS-6956	2.037	$0.05^{+0.46}_{-0.00}$	$0.010^{+9.990}_{-0.000}$	$1.4^{+0.2}_{-0.1}$	$0.56^{+0.62}_{-0.00}$	$43.9^{+402.3}_{-0.0}$	$0.41^{+0.38}_{-0.00}$	$-23.10^{+0.00}_{-0.09}$	$0.08^{+0.13}_{-0.00}$
ECDFS-9822	1.612	$0.10^{+0.30}_{-0.00}$	$0.020^{+1.980}_{-0.005}$	$1.9^{+0.3}_{-0.1}$	$0.68^{+0.29}_{-0.07}$	$25.2^{+270.1}_{-19.0}$	$0.97^{+0.45}_{-0.03}$	$-22.36^{+0.10}_{-0.02}$	$0.50^{+0.05}_{-0.05}$
ECDFS-11490	$2.34^{+0.07}_{-0.02}$	$0.51^{+0.06}_{-0.10}$	$0.065^{+0.015}_{-0.055}$	$0.1^{+0.2}_{-0.1}$	$0.95^{+0.08}_{-0.11}$	$0.7^{+0.6}_{-0.7}$	$0.52^{+0.03}_{-0.06}$	$-23.41^{+0.04}_{-0.07}$	$0.37^{+0.04}_{-0.05}$
ECDFS-12514	2.024	$0.40^{+0.17}_{-0.20}$	$10.000^{+0.000}_{-9.800}$	$1.3^{+0.1}_{-0.1}$	$1.25^{+0.22}_{-0.28}$	$369.1^{+91.7}_{-105.7}$	$0.62^{+0.09}_{-0.12}$	$-23.51^{+0.07}_{-0.03}$	$0.10^{+0.05}_{-0.07}$
ECDFS-13532	2.336	$0.90^{+0.53}_{-0.50}$	$0.250^{+0.750}_{-0.100}$	$1.0^{+0.9}_{-0.5}$	$1.88^{+0.69}_{-0.46}$	$26.8^{+217.2}_{-18.4}$	$1.42^{+0.59}_{-0.35}$	$-23.05^{+0.05}_{-0.02}$	$0.72^{+0.08}_{-0.12}$
ECDFS-16671	$2.61^{+0.02}_{-0.01}$	$0.05^{+0.00}_{-0.00}$	$0.010^{+0.030}_{-0.000}$	$0.9^{+0.4}_{-0.0}$	$1.08^{+0.11}_{-0.05}$	$83.9^{+1081.2}_{-1.0}$	$0.26^{+0.31}_{-0.01}$	$-24.30^{+0.01}_{-0.05}$	$-0.16^{+0.01}_{-0.05}$
CDFS-6202	2.225	$0.20^{+0.08}_{-0.15}$	$0.800^{+9.200}_{-0.790}$	$1.7^{+0.1}_{-0.2}$	$1.26^{+0.16}_{-0.41}$	$649.8^{+145.1}_{-583.6}$	$0.64^{+0.07}_{-0.19}$	$-23.48^{+0.04}_{-0.03}$	$0.16^{+0.03}_{-0.04}$

NOTE. — The stellar population properties are derived by fitting the low resolution spectra together with the optical photometry by Bruzual & Charlot (2003) stellar population models. For the emission-line galaxies the redshift was fixed to  $z_{\text{spec}}$ . The errors represent the 68% confidence intervals derived using 200 Monte Carlo simulations.

<sup>a</sup> The continuum redshifts are those for which we give the confidence intervals.

### 3.2. Photometric Redshifts and Galaxy Properties

Photometric redshifts are derived using the method described by Rudnick et al. (2001, 2003). The code fits a linear non-negative superposition of the 8 templates presented in the left panel of Figure 8 to the broadband photometry using  $\chi^2$  minimization. This template set consist of the empirical E, Sbc, Scd and Im templates from Coleman, Wu & Weedman (1980), the two least reddened starburst templates from Kinney et al. (1996),

and a 1 Gyr and 10 Myr Bruzual & Charlot (2003) single stellar population with a Salpeter (1955) initial mass function (IMF). Confidence intervals on  $z_{\text{phot}}$  are determined using 100 Monte-Carlo simulations, in which the broadband photometry is varied according to the photometric uncertainties.

We determine photometric stellar populations properties by fitting Bruzual & Charlot (2003) stellar population models to the broadband SEDs, with the redshift fixed to the best-fit  $z_{\text{phot}}$ . We apply the same grid and

TABLE 3  
PHOTOMETRIC MODELING RESULTS

ID	$z_{\text{phot}}^a$	age Gyr	$\tau$ Gyr	$A_V$ mag	$M$ $10^{11} M_\odot$	SFR $M_\odot \text{yr}^{-1}$	$M/L_V$ $(M/L_V)_\odot$	V <sup>a</sup>	U-V <sup>a</sup>
1030-32	2.26 <sup>+0.24</sup> <sub>-0.28</sub>	2.20 <sup>+0.55</sup> <sub>-1.80</sub>	0.250 <sup>+0.150</sup> <sub>-0.240</sub>	0.0 <sup>+2.1</sup> <sub>-0.0</sub>	2.35 <sup>+1.81</sup> <sub>-1.09</sub>	0.2 <sup>+10.0</sup> <sub>-0.2</sub>	1.49 <sup>+3.82</sup> <sub>-1.01</sub>	-23.25 <sup>+0.46</sup> <sub>-0.35</sub>	0.91 <sup>+0.71</sup> <sub>-0.28</sub>
1030-101	2.18 <sup>+0.08</sup> <sub>-0.52</sub>	0.90 <sup>+1.50</sup> <sub>-0.62</sub>	0.010 <sup>+0.290</sup> <sub>-0.000</sub>	0.2 <sup>+1.7</sup> <sub>-0.2</sub>	2.70 <sup>+3.51</sup> <sub>-0.76</sub>	0.0 <sup>+15.8</sup> <sub>-0.0</sub>	0.91 <sup>+4.48</sup> <sub>-0.36</sub>	-23.92 <sup>+0.95</sup> <sub>-0.09</sub>	0.72 <sup>+1.39</sup> <sub>-0.15</sub>
1030-301	2.94 <sup>+0.06</sup> <sub>-0.68</sub>	1.01 <sup>+0.59</sup> <sub>-0.30</sub>	0.120 <sup>+0.080</sup> <sub>-0.110</sub>	0.0 <sup>+0.9</sup> <sub>-0.0</sub>	5.21 <sup>+4.39</sup> <sub>-1.05</sub>	1.2 <sup>+11.0</sup> <sub>-1.2</sub>	0.71 <sup>+2.38</sup> <sub>-0.18</sub>	-24.91 <sup>+0.92</sup> <sub>-0.16</sub>	0.53 <sup>+0.31</sup> <sub>-0.00</sub>
1030-609	2.22 <sup>+0.42</sup> <sub>-0.92</sub>	0.51 <sup>+2.24</sup> <sub>-0.50</sub>	0.300 <sup>+9.700</sup> <sub>-0.290</sub>	1.4 <sup>+1.3</sup> <sub>-1.4</sub>	1.59 <sup>+2.26</sup> <sub>-1.19</sub>	148.7 <sup>+4621.8</sup> <sub>-148.3</sub>	0.99 <sup>+15.05</sup> <sub>-0.71</sub>	-23.26 <sup>+2.10</sup> <sub>-0.49</sub>	0.36 <sup>+0.27</sup> <sub>-0.24</sub>
1030-807	2.44 <sup>+0.38</sup> <sub>-0.54</sub>	0.10 <sup>+2.50</sup> <sub>-0.09</sub>	0.030 <sup>+9.970</sup> <sub>-0.020</sub>	2.2 <sup>+0.8</sup> <sub>-2.0</sub>	1.90 <sup>+4.19</sup> <sub>-1.23</sub>	262.5 <sup>+6455.7</sup> <sub>-262.5</sub>	1.02 <sup>+24.17</sup> <sub>-0.76</sub>	-23.42 <sup>+0.86</sup> <sub>-0.47</sub>	0.42 <sup>+0.16</sup> <sub>-0.05</sub>
1030-1531	2.74 <sup>+0.10</sup> <sub>-0.06</sub>	1.28 <sup>+0.92</sup> <sub>-0.87</sub>	1.000 <sup>+9.000</sup> <sub>-0.900</sub>	0.5 <sup>+0.3</sup> <sub>-0.5</sub>	2.64 <sup>+1.71</sup> <sub>-1.57</sub>	131.9 <sup>+149.1</sup> <sub>-107.9</sub>	0.70 <sup>+0.27</sup> <sub>-0.34</sub>	-24.19 <sup>+0.12</sup> <sub>-0.17</sub>	0.17 <sup>+0.17</sup> <sub>-0.19</sub>
1030-1611	2.32 <sup>+0.06</sup> <sub>-0.38</sub>	1.01 <sup>+0.88</sup> <sub>-0.81</sub>	0.150 <sup>+0.150</sup> <sub>-0.140</sub>	0.3 <sup>+1.6</sup> <sub>-0.3</sub>	1.85 <sup>+1.21</sup> <sub>-0.55</sub>	1.9 <sup>+26.7</sup> <sub>-1.9</sub>	0.93 <sup>+0.89</sup> <sub>-0.44</sub>	-23.50 <sup>+0.67</sup> <sub>-0.09</sub>	0.46 <sup>+0.59</sup> <sub>-0.00</sub>
1030-1813	2.32 <sup>+0.16</sup> <sub>-0.16</sub>	0.57 <sup>+1.43</sup> <sub>-0.47</sub>	0.030 <sup>+9.970</sup> <sub>-0.020</sub>	0.7 <sup>+2.3</sup> <sub>-0.7</sub>	3.29 <sup>+11.02</sup> <sub>-0.0</sub>	0.0 <sup>+2417.3</sup> <sub>-0.0</sub>	0.91 <sup>+7.69</sup> <sub>-0.00</sub>	-24.14 <sup>+0.98</sup> <sub>-0.71</sub>	0.17 <sup>+1.06</sup> <sub>-0.00</sub>
1030-1839	2.58 <sup>+0.20</sup> <sub>-0.38</sub>	1.61 <sup>+0.79</sup> <sub>-1.32</sub>	0.800 <sup>+9.200</sup> <sub>-0.720</sub>	1.0 <sup>+0.7</sup> <sub>-1.0</sub>	3.78 <sup>+1.87</sup> <sub>-2.59</sub>	96.2 <sup>+391.7</sup> <sub>-90.5</sub>	1.53 <sup>+2.69</sup> <sub>-1.15</sub>	-23.73 <sup>+0.60</sup> <sub>-0.31</sub>	0.28 <sup>+0.31</sup> <sub>-0.03</sub>
1030-2026	2.68 <sup>+0.10</sup> <sub>-0.30</sub>	1.28 <sup>+0.62</sup> <sub>-0.77</sub>	0.200 <sup>+0.100</sup> <sub>-0.100</sub>	0.0 <sup>+1.6</sup> <sub>-0.0</sub>	2.44 <sup>+3.49</sup> <sub>-0.37</sub>	2.7 <sup>+98.9</sup> <sub>-0.6</sub>	0.79 <sup>+1.97</sup> <sub>-0.36</sub>	-23.97 <sup>+0.35</sup> <sub>-0.13</sub>	0.68 <sup>+0.69</sup> <sub>-0.09</sub>
1030-2329	2.30 <sup>+0.48</sup> <sub>-0.30</sub>	0.20 <sup>+2.55</sup> <sub>-0.15</sub>	0.050 <sup>+9.950</sup> <sub>-0.040</sub>	2.1 <sup>+0.9</sup> <sub>-2.1</sub>	2.25 <sup>+3.98</sup> <sub>-1.13</sub>	96.9 <sup>+2030.0</sup> <sub>-96.9</sub>	1.48 <sup>+10.71</sup> <sub>-1.0</sub>	-23.20 <sup>+0.62</sup> <sub>-0.67</sub>	0.63 <sup>+0.12</sup> <sub>-0.16</sub>
1030-2559	2.18 <sup>+0.34</sup> <sub>-0.20</sub>	0.57 <sup>+2.18</sup> <sub>-0.47</sub>	0.100 <sup>+0.400</sup> <sub>-0.090</sub>	1.6 <sup>+1.4</sup> <sub>-1.6</sub>	2.72 <sup>+2.37</sup> <sub>-1.52</sub>	11.5 <sup>+468.0</sup> <sub>-11.5</sub>	1.96 <sup>+3.73</sup> <sub>-1.54</sub>	-23.10 <sup>+0.39</sup> <sub>-0.46</sub>	0.89 <sup>+0.37</sup> <sub>-0.29</sub>
1030-2728	2.60 <sup>+0.32</sup> <sub>-0.32</sub>	0.20 <sup>+1.23</sup> <sub>-0.15</sub>	0.025 <sup>+9.975</sup> <sub>-0.015</sub>	1.7 <sup>+1.3</sup> <sub>-1.3</sub>	3.19 <sup>+5.46</sup> <sub>-1.36</sub>	4.8 <sup>+3551.5</sup> <sub>-4.8</sub>	1.17 <sup>+2.56</sup> <sub>-0.68</sub>	-23.84 <sup>+0.48</sup> <sub>-0.39</sub>	0.57 <sup>+0.14</sup> <sub>-0.11</sub>
1030-2927	2.26 <sup>+0.24</sup> <sub>-0.52</sub>	0.29 <sup>+2.11</sup> <sub>-0.24</sub>	0.080 <sup>+9.920</sup> <sub>-0.070</sub>	1.6 <sup>+1.0</sup> <sub>-1.6</sub>	2.10 <sup>+2.94</sup> <sub>-0.85</sub>	93.1 <sup>+1673.3</sup> <sub>-93.1</sub>	1.06 <sup>+6.61</sup> <sub>-0.61</sub>	-23.49 <sup>+0.82</sup> <sub>-0.34</sub>	0.50 <sup>+0.14</sup> <sub>-0.12</sub>
1256-0	2.26 <sup>+0.04</sup> <sub>-0.08</sub>	1.01 <sup>+0.12</sup> <sub>-0.51</sub>	0.120 <sup>+0.030</sup> <sub>-0.110</sub>	0.0 <sup>+0.8</sup> <sub>-0.0</sub>	1.90 <sup>+0.78</sup> <sub>-0.16</sub>	0.4 <sup>+2.2</sup> <sub>-0.4</sub>	0.82 <sup>+0.41</sup> <sub>-0.22</sub>	-23.67 <sup>+0.13</sup> <sub>-0.17</sub>	0.65 <sup>+0.01</sup> <sub>-0.02</sub>
1256-142	2.18 <sup>+0.14</sup> <sub>-0.12</sub>	2.20 <sup>+0.55</sup> <sub>-2.00</sub>	0.300 <sup>+0.100</sup> <sub>-0.290</sub>	0.1 <sup>+2.3</sup> <sub>-0.1</sub>	2.76 <sup>+2.03</sup> <sub>-2.33</sub>	0.8 <sup>+86.7</sup> <sub>-0.8</sub>	1.61 <sup>+2.78</sup> <sub>-0.96</sub>	-23.33 <sup>+0.34</sup> <sub>-0.20</sub>	0.92 <sup>+0.45</sup> <sub>-0.18</sub>
1256-519	2.00 <sup>+0.26</sup> <sub>-0.06</sub>	0.20 <sup>+0.94</sup> <sub>-0.10</sub>	0.030 <sup>+0.220</sup> <sub>-0.020</sub>	2.7 <sup>+0.3</sup> <sub>-1.5</sub>	4.94 <sup>+1.58</sup> <sub>-1.49</sub>	23.6 <sup>+549.0</sup> <sub>-23.6</sub>	2.92 <sup>+1.57</sup> <sub>-1.11</sub>	-23.32 <sup>+0.14</sup> <sub>-0.45</sub>	1.34 <sup>+0.31</sup> <sub>-0.64</sub>
1256-1207	2.10 <sup>+0.02</sup> <sub>-0.44</sub>	0.51 <sup>+0.77</sup> <sub>-0.22</sub>	0.030 <sup>+0.120</sup> <sub>-0.020</sub>	1.0 <sup>+0.8</sup> <sub>-1.0</sub>	2.37 <sup>+0.98</sup> <sub>-0.90</sub>	0.0 <sup>+13.6</sup> <sub>-0.0</sub>	1.22 <sup>+2.21</sup> <sub>-0.46</sub>	-23.47 <sup>+0.77</sup> <sub>-0.03</sub>	1.00 <sup>+1.52</sup> <sub>-0.09</sub>
1256-1967	2.16 <sup>+0.06</sup> <sub>-0.72</sub>	0.10 <sup>+0.62</sup> <sub>-0.00</sub>	0.012 <sup>+0.088</sup> <sub>-0.002</sub>	1.9 <sup>+0.2</sup> <sub>-1.9</sub>	3.51 <sup>+0.48</sup> <sub>-1.86</sub>	7.4 <sup>+164.4</sup> <sub>-7.4</sub>	1.03 <sup>+0.46</sup> <sub>-0.65</sub>	-24.08 <sup>+1.34</sup> <sub>-0.09</sub>	0.32 <sup>+0.10</sup> <sub>-0.04</sub>
HDFS1-259	2.24 <sup>+0.76</sup> <sub>-0.18</sub>	0.72 <sup>+2.03</sup> <sub>-0.71</sub>	0.650 <sup>+9.350</sup> <sub>-0.640</sub>	1.4 <sup>+1.3</sup> <sub>-1.4</sub>	2.21 <sup>+3.48</sup> <sub>-1.88</sub>	212.2 <sup>+6029.4</sup> <sub>-212.2</sub>	1.12 <sup>+6.10</sup> <sub>-0.91</sub>	-23.49 <sup>+0.31</sup> <sub>-0.95</sub>	0.35 <sup>+0.07</sup> <sub>-0.23</sub>
HDFS1-1849	2.24 <sup>+0.24</sup> <sub>-0.14</sub>	0.20 <sup>+1.50</sup> <sub>-0.15</sub>	0.040 <sup>+9.960</sup> <sub>-0.030</sub>	2.1 <sup>+0.9</sup> <sub>-1.9</sub>	3.22 <sup>+3.65</sup> <sub>-1.38</sub>	62.6 <sup>+2610.0</sup> <sub>-62.6</sub>	1.59 <sup>+2.75</sup> <sub>-0.83</sub>	-23.52 <sup>+0.23</sup> <sub>-0.37</sub>	0.71 <sup>+0.16</sup> <sub>-0.16</sub>
HDFS2-509	2.78 <sup>+0.40</sup> <sub>-0.04</sub>	0.57 <sup>+1.63</sup> <sub>-0.37</sub>	0.120 <sup>+9.880</sup> <sub>-0.055</sub>	0.5 <sup>+1.5</sup> <sub>-0.5</sub>	5.62 <sup>+17.93</sup> <sub>-2.56</sub>	51.7 <sup>+3051.7</sup> <sub>-43.1</sub>	0.70 <sup>+0.80</sup> <sub>-0.46</sub>	-25.02 <sup>+0.20</sup> <sub>-0.28</sub>	0.30 <sup>+0.05</sup> <sub>-0.27</sub>
HDFS2-1099	2.40 <sup>+0.10</sup> <sub>-0.12</sub>	0.81 <sup>+0.21</sup> <sub>-0.40</sub>	0.120 <sup>+0.030</sup> <sub>-0.070</sub>	0.4 <sup>+0.9</sup> <sub>-0.4</sub>	2.47 <sup>+1.25</sup> <sub>-0.75</sub>	3.2 <sup>+26.0</sup> <sub>-2.5</sub>	0.87 <sup>+0.81</sup> <sub>-0.48</sub>	-23.88 <sup>+0.23</sup> <sub>-0.14</sub>	0.67 <sup>+0.06</sup> <sub>-0.11</sub>
HDFS2-2046	2.36 <sup>+0.14</sup> <sub>-0.10</sub>	0.20 <sup>+0.52</sup> <sub>-0.10</sub>	0.010 <sup>+0.090</sup> <sub>-0.000</sub>	1.2 <sup>+0.8</sup> <sub>-1.2</sub>	2.05 <sup>+0.89</sup> <sub>-0.86</sub>	0.0 <sup>+242.2</sup> <sub>-0.0</sub>	0.88 <sup>+0.16</sup> <sub>-0.46</sub>	-23.67 <sup>+0.15</sup> <sub>-0.25</sub>	0.33 <sup>+0.16</sup> <sub>-0.06</sub>
ECDFS-4454	2.50 <sup>+0.12</sup> <sub>-0.08</sub>	0.72 <sup>+0.19</sup> <sub>-0.00</sub>	0.120 <sup>+0.030</sup> <sub>-0.000</sub>	0.2 <sup>+0.5</sup> <sub>-0.2</sub>	1.94 <sup>+1.28</sup> <sub>-0.38</sub>	5.2 <sup>+16.6</sup> <sub>-2.4</sub>	0.68 <sup>+0.36</sup> <sub>-0.25</sub>	-23.89 <sup>+0.32</sup> <sub>-0.19</sub>	0.83 <sup>+0.69</sup> <sub>-0.53</sub>
ECDFS-4511	2.70 <sup>+0.12</sup> <sub>-0.06</sub>	1.14 <sup>+0.14</sup> <sub>-0.23</sub>	0.250 <sup>+0.050</sup> <sub>-0.050</sub>	0.1 <sup>+0.1</sup> <sub>-0.1</sub>	4.67 <sup>+0.80</sup> <sub>-1.19</sub>	26.0 <sup>+8.5</sup> <sub>-7.3</sub>	0.82 <sup>+0.44</sup> <sub>-0.25</sub>	-24.64 <sup>+0.24</sup> <sub>-0.13</sub>	0.52 <sup>+0.20</sup> <sub>-0.17</sub>
ECDFS-4713	2.30 <sup>+0.36</sup> <sub>-0.04</sub>	1.01 <sup>+1.74</sup> <sub>-0.73</sub>	0.500 <sup>+9.500</sup> <sub>-0.420</sub>	1.0 <sup>+0.5</sup> <sub>-1.0</sub>	5.21 <sup>+7.28</sup> <sub>-3.81</sub>	203.0 <sup>+508.4</sup> <sub>-194.0</sub>	1.26 <sup>+0.89</sup> <sub>-0.92</sub>	-24.29 <sup>+0.14</sup> <sub>-0.48</sub>	0.32 <sup>+0.04</sup> <sub>-0.24</sub>
ECDFS-5856	3.32 <sup>+0.40</sup> <sub>-0.12</sub>	1.61 <sup>+0.09</sup> <sub>-0.80</sub>	0.300 <sup>+0.200</sup> <sub>-0.180</sub>	0.7 <sup>+0.8</sup> <sub>-0.7</sub>	12.20 <sup>+10.70</sup> <sub>-8.30</sub>	25.6 <sup>+177.8</sup> <sub>-21.6</sub>	2.75 <sup>+0.23</sup> <sub>-2.25</sub>	-24.37 <sup>+0.03</sup> <sub>-0.57</sub>	-0.12 <sup>+0.72</sup> <sub>-0.16</sub>
ECDFS-6842	2.96 <sup>+0.04</sup> <sub>-0.64</sub>	0.90 <sup>+1.10</sup> <sub>-0.19</sub>	0.150 <sup>+0.650</sup> <sub>-0.030</sub>	0.2 <sup>+1.3</sup> <sub>-0.2</sub>	4.55 <sup>+16.54</sup> <sub>-1.42</sub>	9.5 <sup>+310.5</sup> <sub>-4.8</sub>	0.77 <sup>+4.62</sup> <sub>-0.30</sub>	-24.68 <sup>+0.76</sup> <sub>-0.12</sub>	0.40 <sup>+0.46</sup> <sub>-0.13</sub>
ECDFS-6956	2.86 <sup>+0.04</sup> <sub>-0.12</sub>	0.90 <sup>+1.10</sup> <sub>-0.10</sub>	0.200 <sup>+0.300</sup> <sub>-0.000</sub>	0.0 <sup>+0.2</sup> <sub>-0.0</sub>	3.14 <sup>+3.46</sup> <sub>-1.17</sub>	22.3 <sup>+20.9</sup> <sub>-0.0</sub>	0.63 <sup>+0.85</sup> <sub>-0.16</sub>	-24.49 <sup>+0.44</sup> <sub>-0.12</sub>	0.36 <sup>+0.78</sup> <sub>-0.42</sub>
ECDFS-9822	2.60 <sup>+0.18</sup> <sub>-0.02</sub>	0.81 <sup>+1.59</sup> <sub>-0.09</sub>	0.150 <sup>+4.850</sup> <sub>-0.030</sub>	0.3 <sup>+1.3</sup> <sub>-0.3</sub>	2.93 <sup>+8.27</sup> <sub>-1.17</sub>	11.8 <sup>+377.4</sup> <sub>-7.0</sub>	0.76 <sup>+2.45</sup> <sub>-0.55</sub>	-24.22 <sup>+0.15</sup> <sub>-0.29</sub>	0.98 <sup>+1.08</sup> <sub>-0.59</sub>
ECDFS-11490	3.58 <sup>+0.14</sup> <sub>-0.68</sub>	0.81 <sup>+0.89</sup> <sub>-0.24</sub>	0.150 <sup>+0.350</sup> <sub>-0.050</sub>	0.0 <sup>+0.8</sup> <sub>-0.4</sub>	4.43 <sup>+15.61</sup> <sub>-2.60</sub>	17.8 <sup>+158.2</sup> <sub>-4.1</sub>	0.61 <sup>+0.88</sup> <sub>-0.41</sub>	-24.91 <sup>+0.55</sup> <sub>-0.47</sub>	0.08 <sup>+1.31</sup> <sub>-0.34</sub>
ECDFS-12514	2.40 <sup>+0.30</sup> <sub>-0.28</sub>	0.51 <sup>+2.09</sup> <sub>-0.50</sub>	0.120 <sup>+9.880</sup> <sub>-0.110</sub>	0.2 <sup>+1.4</sup> <sub>-0.2</sub>	1.87 <sup>+8.11</sup> <sub>-1.71</sub>	28.7 <sup>+2246.3</sup> <sub>-17.2</sub>	0.58 <sup>+2.81</sup> <sub>-0.33</sub>	-24.02 <sup>+0.69</sup> <sub>-0.38</sub>	-0.13 <sup>+0.32</sup> <sub>-0.73</sub>
ECDFS-13532	2.86 <sup>+0.16</sup> <sub>-0.24</sub>	1.28 <sup>+0.92</sup> <sub>-0.37</sub>	0.250 <sup>+0.250</sup> <sub>-0.100</sub>	0.4 <sup>+0.5</sup> <sub>-0.4</sub>	3.83 <sup>+5.14</sup> <sub>-1.99</sub>	12.3 <sup>+34.4</sup> <sub>-8.4</sub>	1.07 <sup>+4.76</sup> <sub>-0.75</sub>	-24.14 <sup>+0.45</sup> <sub>-0.20</sub>	1.29 <sup>+0.64</sup> <sub>-0.64</sub>
ECDFS-16671	3.02 <sup>+0.04</sup> <sub>-0.12</sub>	0.72 <sup>+1.28</sup> <sub>-0.21</sub>	0.250 <sup>+1.750</sup> <sub>-0.100</sub>	0.0 <sup>+0.2</sup> <sub>-0.0</sub>	2.68 <sup>+4.93</sup> <sub>-0.65</sub>	81.9 <sup>+76.4</sup> <sub>-11.4</sub>	0.41 <sup>+0.49</sup> <sub>-0.10</sub>	-24.79 <sup>+0.14</sup> <sub>-0.17</sub>	-0.11 <sup>+0.37</sup> <sub>-0.30</sub>
CDFS-6202	3.04 <sup>+0.06</sup> <sub>-0.64</sub>	0.72 <sup>+0.19</sup> <sub>-0.00</sub>	0.150 <sup>+0.050</sup> <sub>-0.000</sub>	0.0 <sup>+0.2</sup> <sub>-0.0</sub>	3.19 <sup>+0.68</sup> <sub>-0.00</sub>	22.9 <sup>+22.1</sup> <sub>-0.0</sub>	1.45 <sup>+0.00</sup> <sub>-1.02</sub>	-23.60 <sup>+0.03</sup> <sub>-0.06</sub>	0.36 <sup>+0.08</sup> <sub>-0.08</sub>

NOTE. — The stellar population properties are derived by fitting the photometry by Bruzual & Charlot (2003) models, fixing the redshift to  $z_{\text{phot}}$ . The  $z_{\text{phot}}$  confidence intervals are derived using 100 Monte Carlo simulations (Rudnick et al. 2001, 2003). We use the same simulations in combination with the best-fit  $z_{\text{phot}}$  for each simulation to derive the  $1\sigma$  (68%) confidence intervals of the stellar population properties.  
<sup>a</sup> Derived using method by Rudnick et al. (2001, 2003)

reddening law (Calzetti et al. 2000) as for the spectroscopic fitting (§ 3.1). The 100 simulations of the photometry in combination with their best-fit  $z_{\text{phot}}$  are used to derive the confidence intervals on the stellar population properties (see procedure as described in § 3.1).

The errors on the photometric redshifts and rest-frame luminosities are derived independently using the method by Rudnick et al. (2001, 2003). Due to the independent fitting procedures, we do not have a combined  $\chi^2$  distri-

bution for  $M$  and  $L_V$ . For the confidence intervals on  $M/L_V$  we take the minimum and maximum  $M/L_V$  corresponding to the 68% best stellar population fits, i.e., with the lowest  $\chi^2$ . All photometric redshifts, stellar population properties and corresponding confidence intervals are listed in Table 3.

### 3.3. Direct Comparison

In Figure 9 we compare  $z_{\text{spec}}$  and  $z_{\text{phot}}$  for all individual galaxies. We find a scatter of  $\Delta z/(1+z) = 0.13$

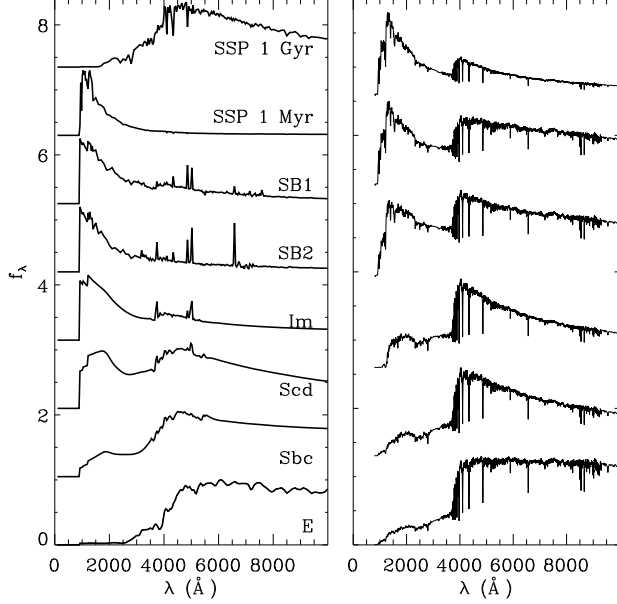


FIG. 8.— *left*: Galaxy templates as used by the original photometric redshift code. *right*: Galaxy templates as constructed from the GNIRS sample.

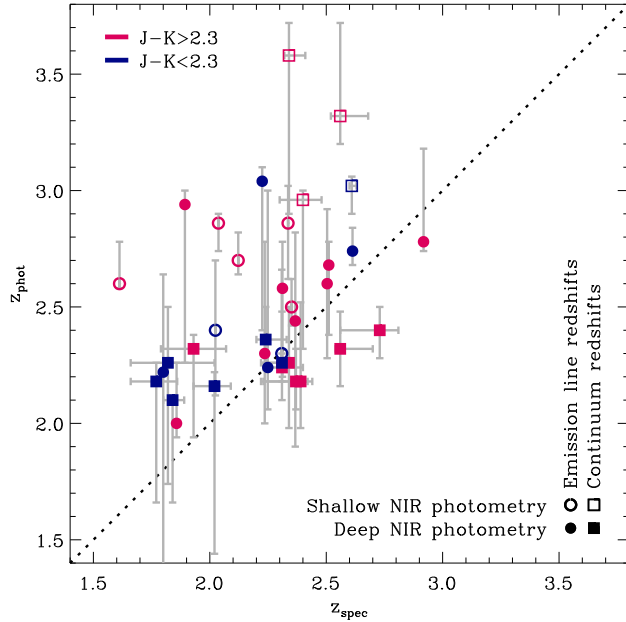


FIG. 9.— Spectroscopic vs. photometric redshifts. The scatter and offset in  $\Delta z/(1+z)$  for the full sample are 0.13 and 0.08 respectively. The squares and circles represent the continuum and emission line redshifts respectively, for galaxies in the deep (filled symbols) and wide (open symbols) MUSYC fields. DRGs ( $J-K > 2.3$ , Franx et al. 2003) are indicated in red and non-DRGs are shown in blue. Corresponding systematic and random errors are given in Table 4.

and a systematic offset of  $\Delta z/(1+z) = 0.08$ , such that our photometric redshifts are on average too high. These values are 0.08 and 0.03 respectively for galaxies in the MUSYC deep fields only (see Table 4). The distributions of the spectroscopic and photometric redshifts for the full and the deep sample, are shown in Figure 10. Using optical spectroscopy and the same photometric redshift

TABLE 4  
COMPARISON BETWEEN PHOTOMETRIC AND SPECTROSCOPIC REDSHIFTS ( $\Delta z/(1+z)$ )

	All		Deep		Wide	
	scat	offs	scat	offs	scat	offs
All	0.13	0.08	0.08	0.03	0.24	0.17
$z_{\text{cont}}$	0.13	0.06	0.10	0.01	0.31	0.21
$z_{\text{lines}}$	0.10	0.07	0.06	0.03	0.24	0.16
DRGs	0.11	0.08	0.07	-0.00	0.32	0.22
DRGs, $z_{\text{cont}}$	0.15	0.01	0.09	-0.05	0.35	0.23
DRGs, $z_{\text{lines}}$	0.07	0.04	0.06	0.03	0.30	0.21
non-DRGs	0.13	0.08	0.13	0.08	0.18	0.12
non-DRGs, $z_{\text{cont}}$	0.13	0.08	0.12	0.08	-	-
non-DRGs, $z_{\text{lines}}$	0.14	0.09	0.16	0.11	0.09	0.06

NOTE. — In this table we give the scatter and systematic offset ( $\Delta z/(1+z)$ ) between the photometric and spectroscopic redshifts for the full sample, and different subsamples.

code and templates, Wuyts et al. (2008) find a scatter of  $\Delta z/(1+z) \sim 0.06$  and a median offset of  $\Delta z/(1+z) \sim 0.02$  for galaxies with deep NIR photometry in the same redshift range. This result is similar to ours when comparing only to the galaxies with deep NIR photometry.

The broadband photometric redshifts of galaxies with emission lines have smaller errors than those of galaxies without emission lines, especially when we exclude the galaxies with shallow NIR photometry. However, our sample is small, and studies of larger spectroscopic samples are needed to verify this result. If this result still holds for larger samples, it probably implies that the quality of photometric redshifts, which are calibrated using just emission-line redshifts, may be overestimated.

The broadband photometric redshifts of galaxies with emission lines have smaller errors than those of galaxies without emission lines (see also Table 4), especially if we exclude the galaxies with shallow NIR photometry. However, our sample is small, and studies of larger spectroscopic samples are needed to verify this result. If this result still holds for larger samples, it probably implies that the quality of photometric redshifts, which are calibrated using just emission-line redshifts, may be overestimated. We stress, however, that galaxies with emission-line and continuum redshifts do not precisely present two distinct classes within this sample, as for certain redshift intervals emission lines are expected to be between atmospheric windows.

Whereas spectroscopic redshifts for blue galaxies can be obtained by optical spectroscopy as well, for most red, optically faint galaxies NIR spectroscopy offers the only possibility to obtain a  $z_{\text{spec}}$ . Previous studies, our photometric redshift estimates among them, were mainly calibrated using optical spectroscopy. Therefore, it is interesting to know whether red and blue high-redshift galaxies show similar scatter and systematics. We divide the full sample into two classes using the DRG criterion ( $J-K > 2.3$ , Franx et al. 2003). In Figure 9 we indicate the DRGs and non-DRGs by red and blue symbols respectively. We find no significant difference in the scatter or systematic offset in  $\Delta z/(1+z)$  for blue and red galaxies for the total sample. When only considering the galaxies

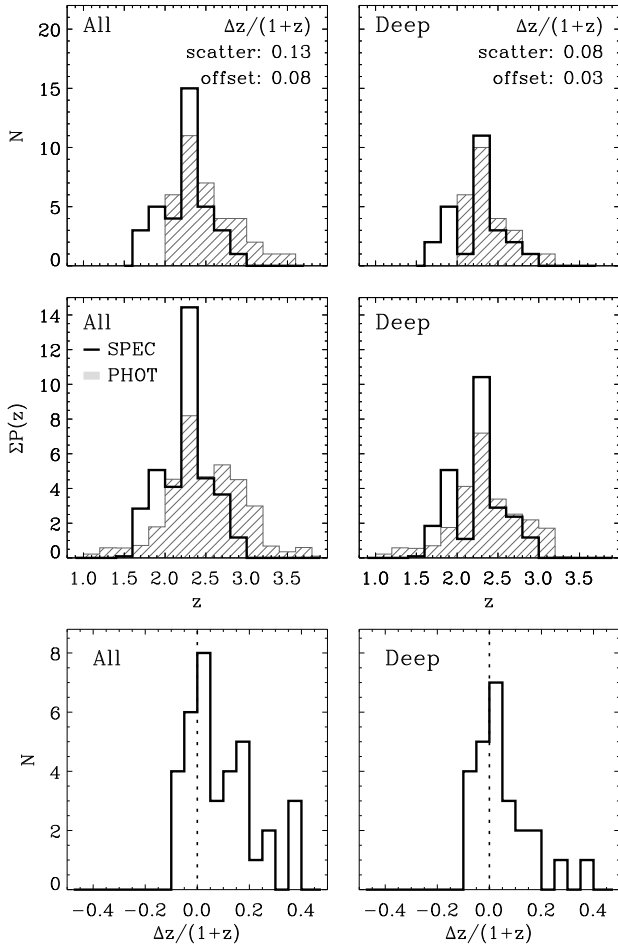


FIG. 10.— Spectroscopic (black solid histograms) and photometric (diagonally hatched histograms) redshift distributions (top panels) and their summed probability distributions (middle panels) for the full spectroscopic sample (left panels), and for those galaxies with deep NIR photometry (right panels). The scatter and systematic offset in  $\Delta z/(1+z)$  are given in the top right corner in the top two panels. The lower panels show the distribution of  $\Delta z/(1+z)$  for the full (left) and deep (right) sample respectively.

with deep NIR photometry, DRGs seem to have more accurate photometric redshifts than non-DRGs. We note, however, that due to the redshift dependence of the  $J-K$  color (see Fig. 2), the trend between  $\Delta z/(1+z)$  and  $z_{\text{spec}}$  (which is a logical result of our  $z_{\text{phot}}$  selection) complicates the interpretation of this test. In the next section we will use rest-frame colors in order to avoid this effect.

### 3.4. Systematics and Catastrophic Failures

In this section we will examine the different causes for systematics and catastrophic failures in  $\Delta z/(1+z)$  as identified in the previous subsection. We define failures as galaxies for which  $\Delta z/(1+z) > 0.1$ . In Figure 11 we show the broadband photometry and best-fit stellar population models, in- or excluding the spectral information, for all failures. However, for several galaxies the photometric redshift is poorly constrained – for example due to degeneracies – and despite the large discrepancy,  $z_{\text{spec}}$  agrees reasonably well with the confidence interval of  $z_{\text{phot}}$ . Thus we discriminate between failures for which  $z_{\text{spec}}$  is or is not consistent within  $3\sigma$  with  $z_{\text{phot}}$ , and define these as “good failures” and “bad failures”

respectively. This is illustrated in Figure 12a, in which we show  $\Delta z/(1+z)$  versus the difference between  $z_{\text{phot}}$  and  $z_{\text{spec}}$  in  $\sigma$ . For one galaxy with  $\Delta z/(1+z) < 0.1$  (1256-519),  $z_{\text{phot}}$  and  $z_{\text{spec}}$  are not consistent within  $3\sigma$ .

Figure 12b shows that all bad failures have shallow NIR photometry, with an average S/N in  $H$  and  $K$  of  $< 10$ . This illustrates that deep NIR photometry is needed to get meaningful photometric redshifts and corresponding confidence intervals. Not all galaxies with shallow NIR photometry are bad failures, or even failures at all, but the probability that a galaxy with shallow NIR data has a  $z_{\text{phot}}$  which is inconsistent with the spectroscopic redshift is substantially larger than for galaxies with deep NIR data.

As good failures have similar  $\Delta z/(1+z)$  as bad failures, their confidence intervals are by definition larger. Large confidence intervals may be caused by shallow NIR data or model degeneracies. Several good failures indeed have shallow NIR photometry, and their photometric redshifts are – possibly by coincidence – consistent with their spectroscopic redshifts. The deviating photometric redshifts of high S/N failures must have a different origin. In the following we examine several potential causes for good failures:

*Deviating NIR colors:* In Figure 12c we relate  $(z_{\text{phot}} - z_{\text{spec}})/(1 + z_{\text{spec}})$  with the difference between the photometric and spectroscopic  $J-H$  color (see §2.2). As the optical break falls between the  $J$ - and  $H$ -band for  $z = 2-3$  galaxies, a deviating  $J-H$  color may affect the optical break identification, and thus may place a galaxy at the wrong redshift. This may have happened for 1030-609 and 1030-2927 (see Fig. 5). We note that a few galaxies are missing from Figure 12c as their spectroscopic NIR colors could not be determined (see Fig. 4).

*Emission-line contamination:* Contamination by emission lines generally reddens the rest-frame optical colors, which may result in a wrong break identification. Figure 12d shows that for several galaxies the photometric NIR colors appear redder due to the flux contribution by emission lines. However, there is only one galaxy (CDF5-6026, see Fig. 5) with deep NIR photometry, for which the emission line contamination may be the main cause for a wrong  $z_{\text{phot}}$ .

*K band magnitude:* Due to the shape of the luminosity function, the fraction of low to high redshift galaxies is much larger at brighter  $K$  magnitudes. Thus, it is expected that the interloper fraction is larger at the bright end. In Figure 12e we indeed see that the fraction of good failures compared to the total sample increases at brighter  $K$  magnitudes. This effect can be reduced by using a luminosity prior in the  $z_{\text{phot}}$  fitting code, to break the degeneracy in favor of the correct low-redshift solution.

*Correlations with SED types:* In Figures 12f, g and h we examine correlations with SED type by comparing  $(z_{\text{phot}} - z_{\text{spec}})/(1 + z_{\text{spec}})$  with rest-frame  $U-V$  color, best-fit age and dust content (all derived from the spectroscopic information). We use rest-frame  $U-V$  colors, instead of observed  $J-K$  colors, as the latter are dependent on redshift (see § 3.3). We find no obvious correlation between  $(z_{\text{phot}} - z_{\text{spec}})/(1 + z_{\text{spec}})$  and rest-frame  $U-V$  color. Nonetheless, Figures 12g and h suggest a relation with stellar population properties, such that young

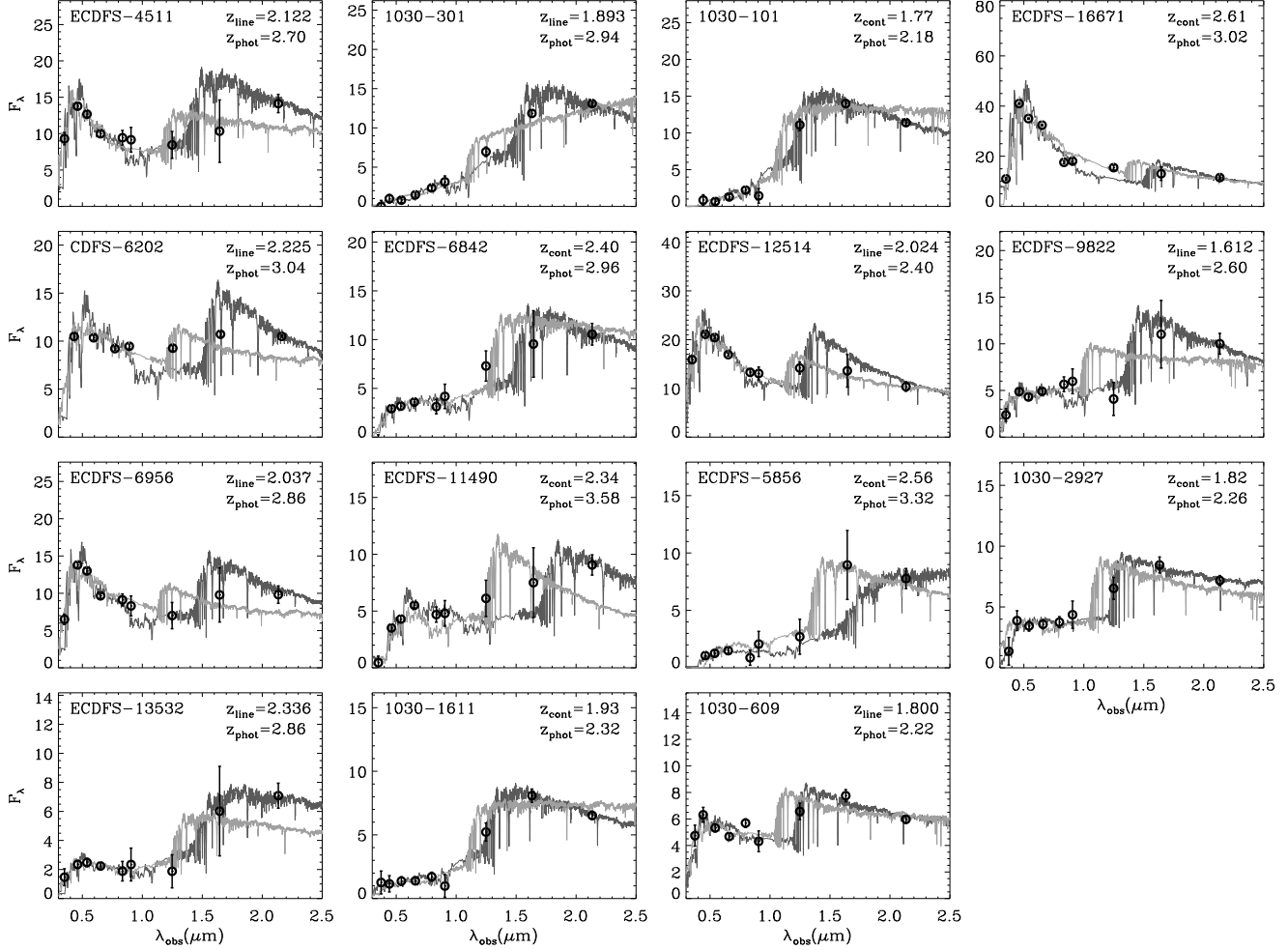


FIG. 11.— Broadband photometry of all galaxies for which the photometric and spectroscopic redshifts are substantially different ( $\Delta z/(1+z) > 0.1$ ). The dark gray fit shows the best-fit stellar population model to just the broadband photometry. The best-fit stellar population model to the spectrum in combination with the optical photometry is presented by the light gray fit. Both the photometric and spectroscopic (emission-line or continuum) redshifts are given in the panels.

and/or dusty galaxies have a higher probability of having a wrong  $z_{\text{phot}}$ . These galaxies are in our photometric redshift code generally best-fit by the 1 Gyr dust-free template (Fig. 8), which places them at the wrong redshift (see also § 4.1). One of these galaxies is 1256-519, for which  $z_{\text{phot}}$  and  $z_{\text{spec}}$  are not consistent within  $3\sigma$  (although  $\Delta z/(1+z) < 0.1$ ). This may suggest that appropriate templates (i.e., dusty ones) are missing in our  $z_{\text{phot}}$  procedure. We will examine this in more detail in § 3.5.

All discussed potential causes generally overestimate photometric redshifts, and place the galaxy at too high redshift. Altogether, this introduces a systematic effect. In the next section we will examine the influence of the different causes, by attempting to correct for them.

### 3.5. An Empirically-Motivated Template Set

In order to test the different causes found for the systematics and failures in  $\Delta z/(1+z)$ , we refit the photometry attempting to correct for these effects. First we construct a new template set from our GNIRS sample. By eye we pick six best-fit SEDs from Figure 5, to be representative for the  $z \sim 2.5$  massive galaxy population. These new templates are presented in the right

panel of Figure 8. We refit the broadband photometry of all galaxies only allowing these 6 templates, without superposition and luminosity prior, in steps ( $\Delta z$ ) of 0.02.

In Figures 13a and b we show the comparison between the old and new  $z_{\text{phot}}$ , respectively, versus  $z_{\text{spec}}$ . The galaxies with high S/N NIR photometry are presented by filled symbols. The new templates reduce both the systematics and scatter. Remarkably, the improvement is largest for galaxies with low S/N photometry.

Although, the newly defined template set yields more accurate photometric redshifts than the original template set, it provides no general solution. It is constructed to work especially for massive galaxies at  $2 < z < 3$ , and thus they may not be appropriate when applied to lower redshift or less massive galaxies. Nevertheless, this test illustrates the importance of using well-calibrated templates. Similar template mismatches may also apply to other galaxy populations, and further exploration is needed in order to better calibrate high-redshift studies.

In order to test whether errors in the NIR broadband photometry may be responsible for systematics or may lead to an increase in the scatter, we attempt to correct the photometry using the NIR spectra. In Figure 13c we replace the  $J$ ,  $H$  and  $K$  by the spectroscopic col-

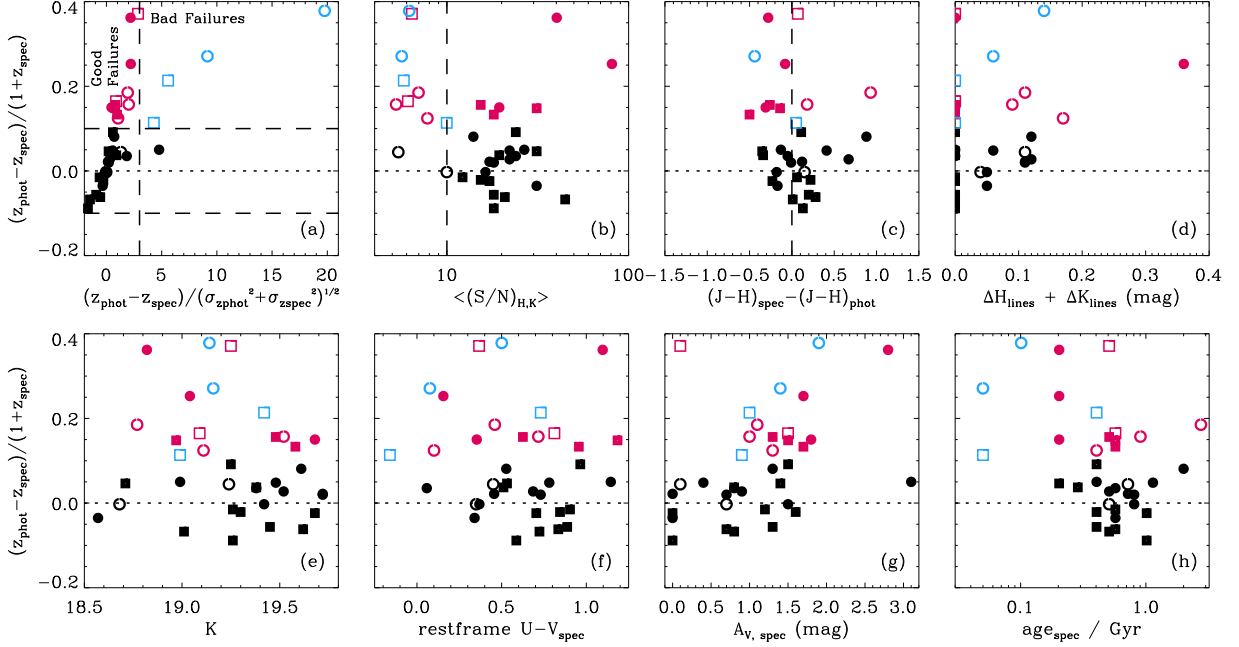


FIG. 12.— In this figure we examine systematics and catastrophic failures in  $\Delta z/(1+z)$ . Squares and circles represent galaxies with continuum and emission-line redshifts respectively, in the wide (*open symbols*) and deep (*filled symbols*) MUSYC surveys. Galaxies with  $\Delta z/(1+z) < 0.1$  are represented by the black symbols. In panel *a* we classify failures ( $\Delta z/(1+z) > 0.1$ ) such that galaxies for which  $z_{\text{spec}}$  is within  $3\sigma$  consistent with  $z_{\text{phot}}$  are defined as “good failures” (*red*), while galaxies that do not meet this criterion are defined as “bad failures” (*blue*). Furthermore, we relate  $(z_{\text{phot}} - z_{\text{spec}})/(1 + z_{\text{spec}})$  with the S/N of the NIR photometry (*b*), the difference between the photometric and spectroscopic  $J - H$  colors (*c*), the contamination of the broadband photometry by emission lines (*d*), total  $K$ -band magnitude (*e*), rest-frame  $U - V$  color (*f*), and the stellar population properties  $A_V$  (*g*) and age (*h*). This figure illustrates that  $(z_{\text{phot}} - z_{\text{spec}})/(1 + z_{\text{spec}})$  is generally larger for galaxies with shallow NIR photometry, and mainly correlates with SED type.

ors and repeat the original fitting procedure, using the original templates. The spectroscopic colors do not lead to an improvement, and in fact even lead to more pronounced scatter and systematics, in particular for the galaxies with deep NIR photometry. This might not be surprising, as for these galaxies the S/N of the  $J - H$  photometric colors is generally higher than the S/N of the spectroscopic colors.

Furthermore, we remove the emission line fluxes from the broadband photometry before repeating the original fitting procedure. Figure 13d shows that this does not reduce the scatter or the systematics. This may be because several of the original templates contained emission lines. Also, the massive galaxies studied in this work all have comparatively weak emission lines, and contamination may play a much larger role for less massive galaxies.

#### 4. IMPLICATIONS

The spectroscopic redshifts and higher resolution spectral shapes as obtained by the NIR spectra provide better constraints on the stellar population properties. This allows us to test the significance and reliability of the photometrically derived properties, and examine the completeness and systematics of photometric samples. In § 4.1 we quantify the improved constraints on the stellar population properties, and identify the driving force behind this improvement. In § 4.2 we test photometric samples, and finally in § 4.3 we assess previous studies based on photometric samples.

##### 4.1. Implications for Derived Properties

In this section we compare the photometric and spectroscopic stellar population properties, as listed in Ta-

bles 2 and 3. Note that the photometric properties are derived using the original photometric redshifts (§ 3.2). Figure 14 illustrates the effect on the properties age,  $A_V$ ,  $\tau$ , stellar mass and SFR when including the spectroscopic information. In the left panels we show the comparison for individual galaxies. The panels in the second column present the distributions of the photometric and spectroscopic properties. In the third column we show the distribution of the difference between photometric and spectroscopic properties. Finally, in the panels in the fourth column we show the ratio of the photometric and spectroscopic  $1\sigma$  confidence intervals.

The differences between the best-fit photometric and spectroscopic properties in the left diagrams of Figure 14 are striking.  $A_V$  has a scatter of  $\sim 1$  mag, and age,  $\tau$  and SFR each have a scatter of a factor of  $\sim 3$ -4, between the photometric and spectroscopic values. Despite the large scatter, for a high fraction (75-89%) of the galaxies the photometric properties are consistent with the spectroscopic properties within  $1\sigma$ . This demonstrates the reliability of the large confidence intervals in Table 3, and supports that the best-fit photometric properties age,  $A_V$ ,  $\tau$  and SFR are poorly determined for individual galaxies. The spectroscopic properties are better constrained, but the errors are still substantial, with a factor of  $\sim 2$  for age, tau, and SFR and  $\sim 0.4$  mag for  $A_V$ . Thus, it is not surprising that the stellar population properties show a large scatter, even when the photometric redshift is close to the spectroscopic redshift.

Although the photometrically and spectroscopically derived best-fit values are consistent, the photometric and spectroscopic distributions show systematic differences (Fig. 14, 2nd column). In § 3.4 we identified possi-

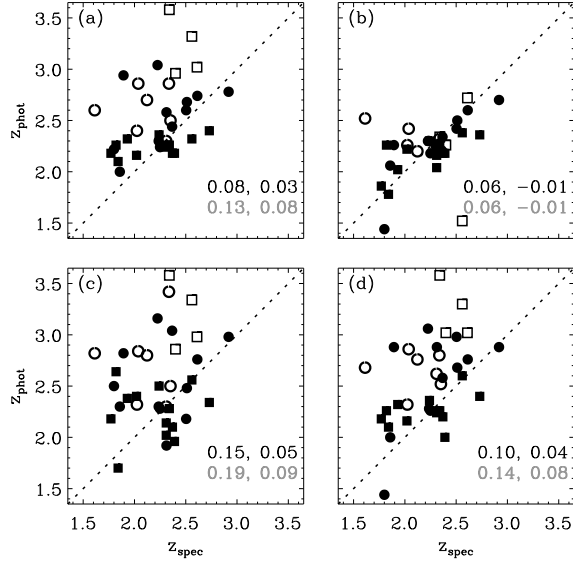


FIG. 13.— In this figure we test the different causes for scatter and systematics in  $\Delta z/(1+z)$ . In panels *a* we show the original  $z_{\text{phot}}$  and in panels *b* we use the new templates as shown in Figure 8 to derive photometric redshifts. In panel *c* we have repeated the original fitting procedure, replacing the NIR photometry by the spectroscopic *J*, *H* and *K* fluxes. In panel *d* we remove the emission line fluxes from the broadband photometry before applying the photometric redshift procedure. Circles and squares represent galaxies with emission line and continuum redshifts respectively. For galaxies with deep NIR photometry the symbols are filled. The scatter and systematic in  $\Delta z/(1+z)$  are given in black for the high S/N galaxies and in gray for the total sample. This figure illustrates that the systematic offset in  $z_{\text{phot}}$  can almost completely be removed and the absolute errors reduced by using well calibrated templates.

ble correlations between  $\Delta z/(1+z)$  and stellar population properties. Due to the lack of appropriate templates, the stellar population properties seem to “converge” to the properties of the template that provides the best fit during the  $z_{\text{phot}}$  procedure. As many galaxies are best-fit by the dust-free 1 Gyr template, we see a peak at  $A_V = 0$  and an age of 1 Gyr for the photometry. The  $A_V = 0$  peak completely disappears, and the age peak shifts to lower ages when including spectroscopic information. This suggest that the distribution of best-fit photometric stellar population properties, as presented in the 2nd column of Figure 14 may be strongly biased.

While it is clear that spectroscopic data significantly improve the constraints on the stellar population properties, it is interesting to know whether the improvements are primarily due to the precise redshift determination or whether they are also caused by the spectroscopic measurement of the continuum shape. We test the impact of both effects by modeling the broadband photometry by stellar population models (see procedure § 3.1), fixing the redshift to  $z_{\text{spec}}$ . In Figure 15 we disentangle the two effects, by comparing on the horizontal axis the improvement of the stellar population properties due to the higher resolution spectral shape (i.e., new modeling results versus spectroscopic properties) and on the vertical axis the effects of the better constrained redshift (i.e., photometric properties versus new modeling results). The corresponding scatter and systematics are listed in Table 5. Remarkably, the results for age and  $\tau$  are more affected by the higher resolution spectral shape,

TABLE 5  
COMPARISON BETWEEN PHOTOMETRICALLY AND SPECTROSCOPICALLY DERIVED PROPERTIES

Quantity		$Q_{\text{ph}}(z_{\text{ph}})$ vs. $Q_{\text{sp}}(z_{\text{sp}})$		$Q_{\text{ph}}(z_{\text{ph}})$ vs. $Q_{\text{ph}}(z_{\text{sp}})$		$Q_{\text{ph}}(z_{\text{sp}})$ vs. $Q_{\text{sp}}(z_{\text{sp}})$	
		offs	scat	offs	scat	offs	scat
age	all	1.22	2.70	1.00	1.76	1.06	2.67
	deep	1.04	2.55	1.02	1.69	1.01	2.73
$A_V$	all	-0.34	1.03	-0.30	0.59	0.05	0.47
	deep	-0.12	0.88	-0.11	0.35	-0.02	0.45
$\tau$	all	0.89	4.18	0.93	3.00	1.00	4.77
	deep	0.80	3.13	0.82	2.11	0.76	5.74
mass	all	1.38	2.23	1.11	1.78	1.14	1.89
	deep	1.28	2.05	1.11	1.72	1.06	1.78
SFR	all	0.81	4.13	0.83	4.13	0.98	2.63
	deep	0.88	3.51	0.94	3.49	0.78	3.00
$M/L_V$	all	1.05	2.06	0.97	1.78	1.09	1.75
	deep	1.00	1.93	0.98	1.76	1.05	1.77
$V$	all	-0.38	0.60	-0.34	0.56	-0.01	0.07
	deep	-0.21	0.40	-0.19	0.38	-0.00	0.04
$(U - V)$	all	-0.06	0.30	-0.06	0.21	0.02	0.08
	deep	-0.08	0.20	-0.06	0.14	0.01	0.06

NOTE. — In this table we list for all properties the scatter and systematic offset between the photometrically and spectroscopically derived properties ( $Q_{\text{ph}}(z_{\text{phot}})$  vs.  $Q_{\text{sp}}(z_{\text{spec}})$ ). Furthermore, we examine whether this scatter between the photometric and spectroscopic properties is mainly driven by the precise redshift measurement ( $Q_{\text{ph}}(z_{\text{phot}})$  vs.  $Q_{\text{ph}}(z_{\text{spec}})$ ), or the higher resolution spectral shape ( $Q_{\text{ph}}(z_{\text{spec}})$  vs.  $Q_{\text{sp}}(z_{\text{spec}})$ )

rather than by the better constrained redshift. For SFR and  $A_V$  both effects are equally important.

Photometric stellar mass is significantly better constrained, with a scatter of  $\sim 2$ . Nevertheless, this property is generally overestimated by a factor of  $\sim 1.4$ . Even if we exclude the galaxies with low S/N NIR photometry, we still obtain photometric stellar masses which are on average a factor of  $\sim 1.3$  too high. This overestimation is lower than the factor of 2 found by Shapley et al. (2005) for blue galaxies. However, the values are not directly comparable, as their mass ratio is derived by using spectroscopic or photometric redshifts when fitting *UGRK* and *IRAC* photometry. In Figure 15 we find that the improved constraints on stellar mass is evenly driven by a better constrained redshift and the higher resolution spectral shape (see also Table 5). Thus, spectroscopic redshifts combined with broadband photometry may still overestimate the stellar mass, although by a small factor of  $\sim 1.1$ .

In Figure 14 we also show the comparison between the photometrically and spectroscopically derived  $M/L_V$ , rest-frame magnitude  $V$  and rest-frame  $U - V$  color. Of all photometric properties  $M/L_V$  is the best determined, and shows no systematic offset. Rest-frame  $U - V$  colors are in general underestimated by  $\sim 0.1$  mag, and show a scatter of  $\sim 0.2$  for the galaxies with deep NIR photometry. Figure 15 shows that the systematics and scatter are mainly due to the lack of a spectroscopic redshift. This effect is even worse for rest-frame  $V$  magnitudes. As expected, rest-frame  $V$  magnitudes can very accurately be determined once the redshift is known. Thus, for photometric redshifts this quantity is less well constrained with an offset of  $\sim 0.2$  and a scatter of  $\sim 0.4$  for the deep NIR photometry.

Better constrained properties and confidence inter-

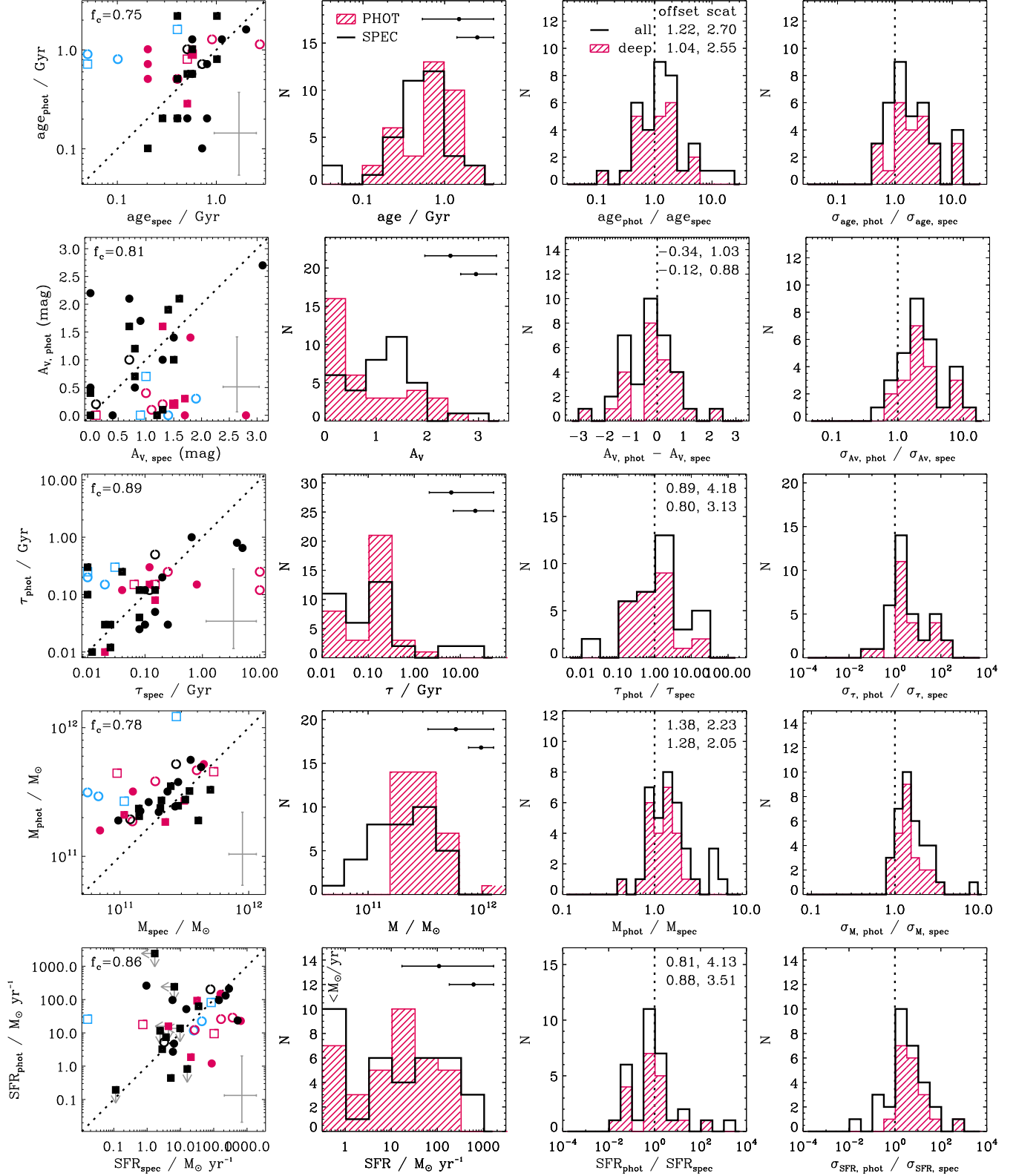
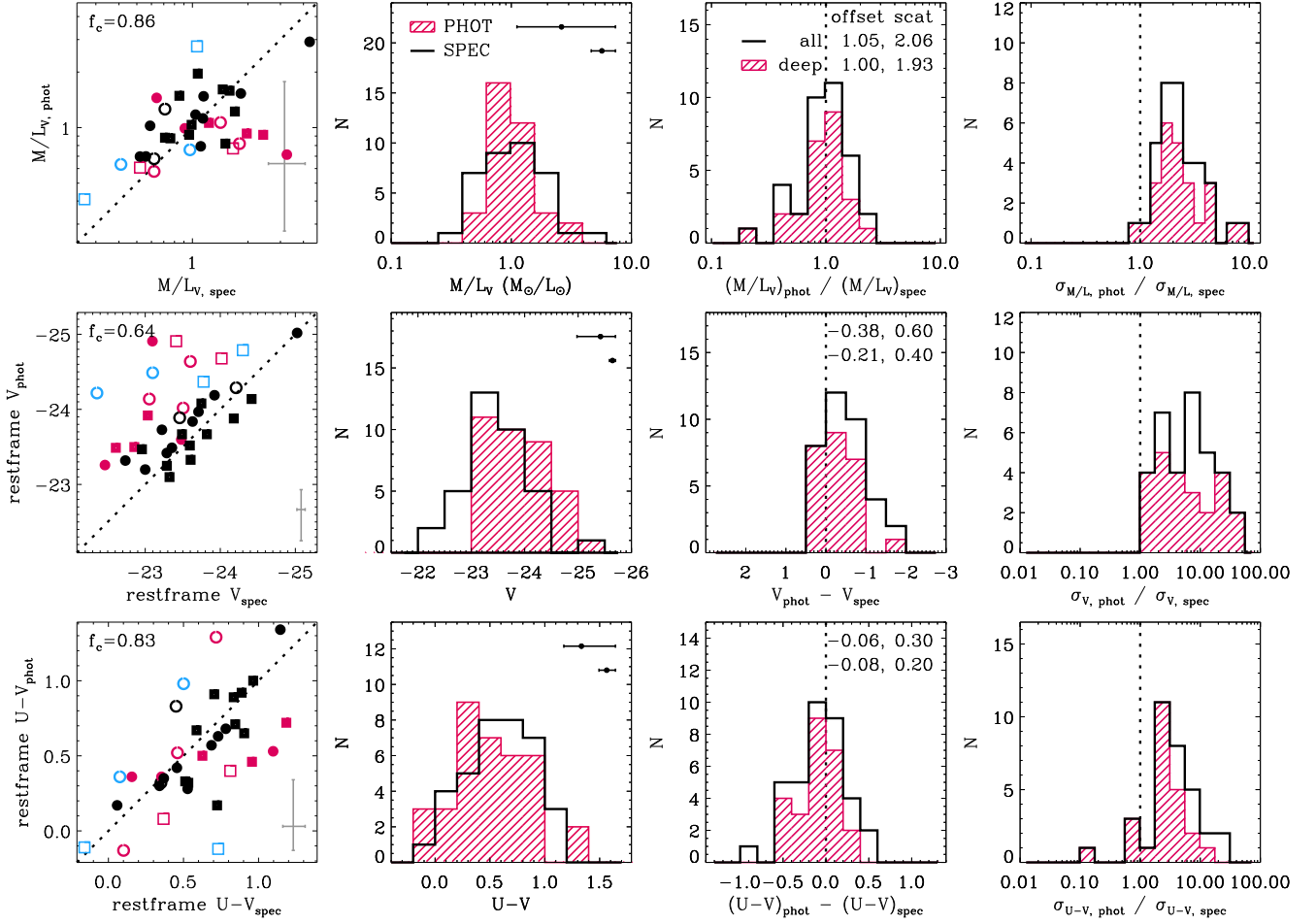


FIG. 14.— Comparison of the photometric and spectroscopic properties age (since the onset of star formation),  $A_V$ ,  $\tau$ , stellar mass, SFR,  $M/L_V$  ratio, rest-frame V magnitude, and rest-frame U-V color. The left panels show the direct comparison for the individual galaxies with the symbols similar as in Figure 12. The fraction ( $F_c$ ) of galaxies for which the photometric and spectroscopic properties are consistent within  $1\sigma$  is given in the top left corner, and the typical error in the bottom right. The dotted diagonal lines indicate where the spectroscopic properties are equal to the photometric properties. The panels in the second column show both distributions. The typical errors for the photometric and spectroscopic properties is presented in the top right corner. The distribution of the difference (normalized biweight mean absolute deviation) of the distribution is given for each property for the total and deep sample. In the right panels we present the distribution of the ratio of the photometric and spectroscopic confidence intervals for the individual galaxies. The black histograms represent all galaxies, and the colored, diagonally hatched areas correspond to the galaxies with deep NIR photometry. This figure illustrates that the stellar population properties such as the age,  $A_V$ , SFR, and  $\tau$  are generally very poorly constrained with broadband data alone. Interestingly, stellar masses and  $M/L_V$  are among the most stable properties.

FIG. 14.— *Continued*

vals can also be obtained by extending the broadband SEDs by mid-infrared Spitzer/IRAC photometry (e.g., Labbé et al. 2005; Wuyts et al. 2007). Wuyts et al. (2007) show that the distribution of stellar population properties does not change significantly when IRAC data are added to their *UBVIJHK* photometry. However, for individual galaxies the addition of IRAC can improve the constraints on the stellar populations significantly. As we do not have photometric catalogs including the IRAC bands for the GNIRS galaxies yet, it is difficult to examine whether the IRAC bands have a similar effect as the higher resolution spectral shape on the stellar population properties.

Finally, we stress that the derived photometric and spectroscopic properties are not completely independent, as we use the same optical photometry for both, and the NIR spectra are calibrated using the NIR photometry. Furthermore, the confidence levels do not include all uncertainties, as all photometrically and spectroscopically derived stellar population properties are based on the same assumptions, among which a Salpeter (1955) IMF, solar metallicity, an exponentially declining SFH, and the Bruzual & Charlot (2003) stellar population models.

#### 4.2. Implications for Photometric Samples

In the previous section we examined the improvement of stellar population properties when including the spec-

troscopic information. However, due to the different redshift distributions, the photometric and spectroscopic properties as presented in Figure 14 should not be compared directly to examine the implications for galaxy samples. Due to degeneracies between redshift and stellar population properties, the systematic effects may even be worse for complete samples, than for individual galaxies. Thus, it is important to consider the same redshift interval in order to examine the systematics of photometric samples.

In the top panels of Figure 16 we show the photometric and spectroscopic properties stellar mass, rest-frame  $U-V$  color, and observed  $J-K$  and  $R-K$  color versus redshift of the total GNIRS sample. The photometrically derived properties are presented by open diamonds and the filled squares represent the spectroscopically derived properties. Hence, all galaxies are shown twice. This figure illustrates how photometric and spectroscopic properties of galaxies in a certain redshift interval differ, and which galaxies fall out and in the targeted redshift interval ( $2.0 < z < 2.7$ ) when spectroscopic information is included. For example, several of the galaxies for which the photometric redshift and hence stellar mass were substantially overestimated, move to  $z < 2$ , and thus will not have a large effect on the properties of the  $2.0 < z < 2.7$  sample. We note, however, that our spectroscopic sample is not complete, as galaxies with

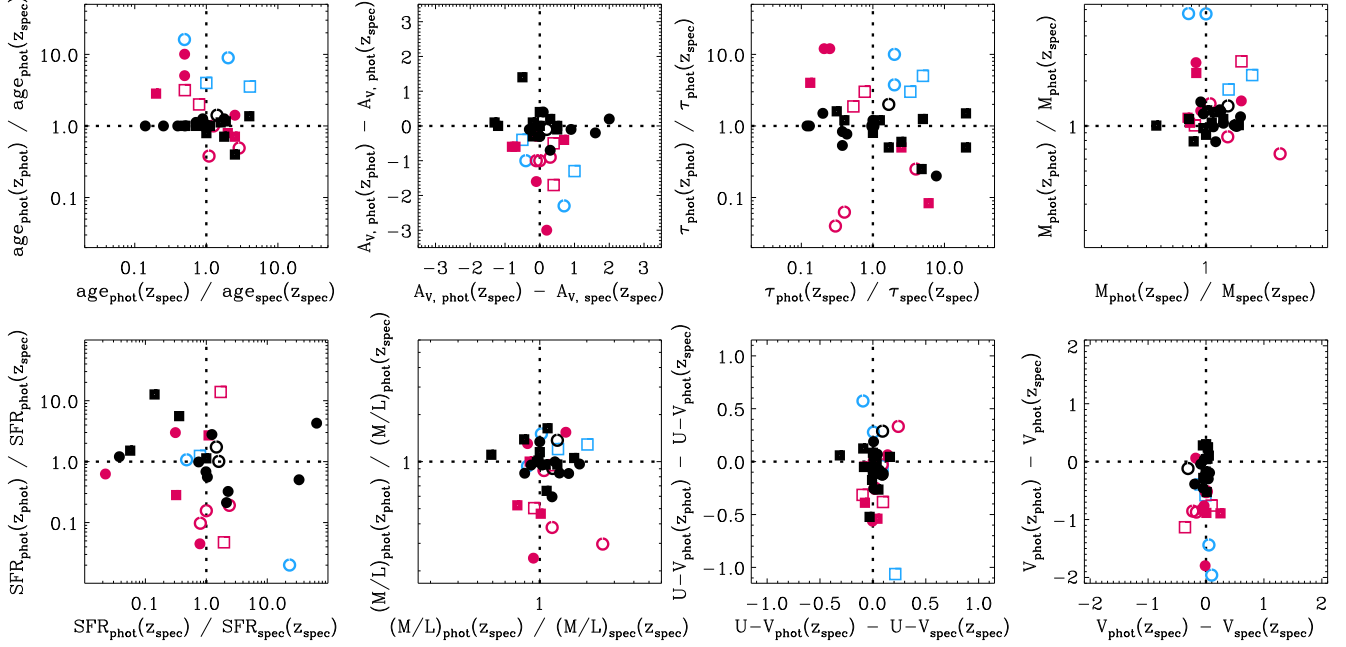


FIG. 15.— In this figure we examine the influence of both the better constrained redshift and the higher resolution spectral shape on the stellar population properties (see also Table 5). The y-axes present the difference between best-fit properties by including spectroscopic redshifts. We derived this improvement by fitting the photometry replacing  $z_{\text{phot}}$  by  $z_{\text{spec}}$ . On the x-axes we show the additional improvement due to the higher resolution spectral shape. This improvement is the difference between the best-fit values for fitting the photometry with the redshift fixed to  $z_{\text{spec}}$ , in- and excluding the NIR spectrum. Symbols are similar as in Figure 12.

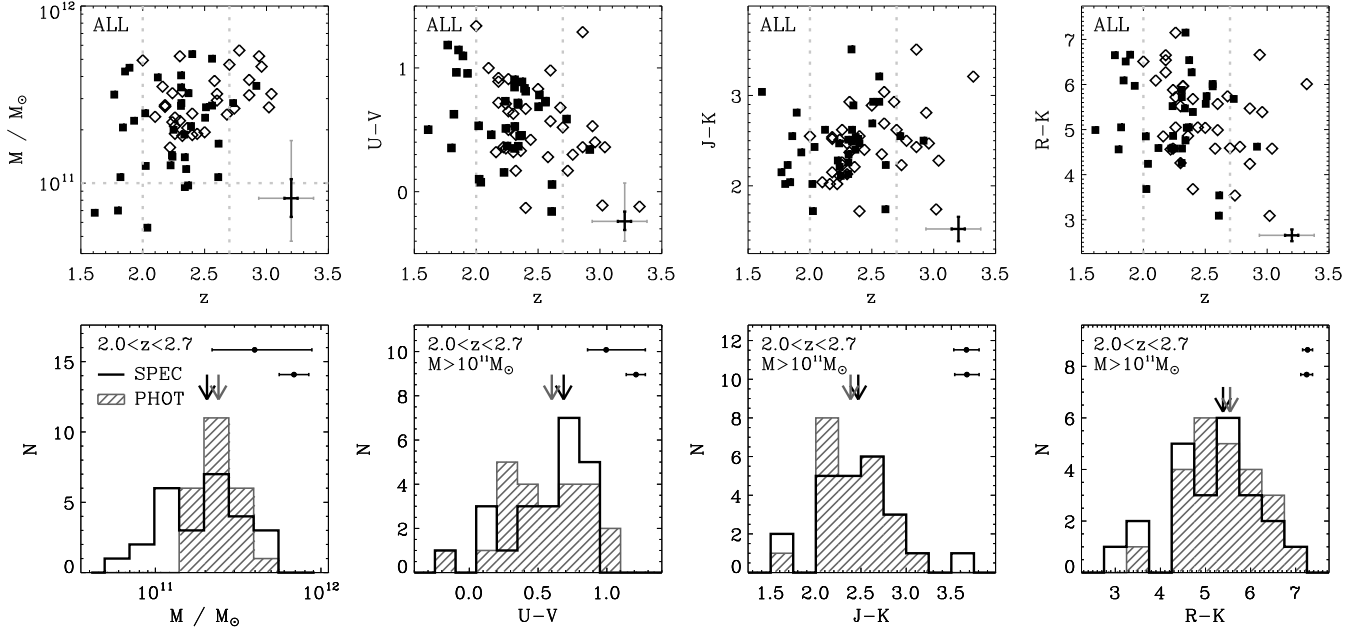


FIG. 16.— Comparison of photometrically (*open diamonds*) and spectroscopically (*filled squares*) derived properties of the full spectroscopic sample. The top panels show stellar mass, rest-frame  $U - V$  color, observed  $J - K$  and  $R - K$  color versus redshift. Hence all galaxies are plotted twice. The  $J - K$  and  $R - K$  colors are in both cases photometric, while for the other properties ( $z$ ,  $U - V$  and stellar mass) we adopt the spectroscopic or photometric values. The bottom panels show for both the distribution of the stellar mass, rest-frame  $U - V$  color, observed  $J - K$  and  $R - K$  color for galaxies in the same redshift range, and for the latter three, the same mass range. The arrows indicate the median values of the distributions. The typical errorbars are shown in the bottom and top right of the top and bottom panels respectively. The barely changed distributions of  $J - K$  and  $R - K$  imply that the spectroscopy supports the previous finding that red galaxies dominate the high mass end at  $2 < z < 3$ .

$z_{\text{phot}} < 2.0$  and  $z_{\text{phot}} > 2.7$  may scatter into the spectroscopic sample. Although the photometric sample contains 10 galaxies with  $z_{\text{phot}} > 2.7$ , these galaxies may not be representative for all galaxies with  $z_{\text{phot}} > 2.7$

and  $2.0 < z_{\text{spec}} < 2.7$ .

In the bottom panels in Figure 16 we compare the photometric and spectroscopic distributions of stellar mass,  $J - K$ ,  $R - K$  and rest-frame  $U - V$  of the  $2.0 < z < 2.7$

galaxy sample. The first panel illustrates that photometric stellar masses in general are slightly overestimated. In order to compare how the properties of a mass-limited sample would change, we use a mass-cut of  $> 10^{11} M_{\odot}$  ( $M_{\text{spec}}$  for the “spectroscopic” sample and  $M_{\text{phot}}$  for the “photometric” sample) in addition to the redshift interval for the remaining properties. The second panel demonstrates that spectroscopically derived rest-frame  $U - V$  colors of a mass-limited sample at  $2.0 < z < 2.7$  are slightly redder ( $\sim 0.1$  mag) than inferred from just the photometry. Furthermore, the distribution is peaked around  $U - V \sim 0.75$ , possibly indicating a red sequence (M. Kriek et al. 2007 in preparation). Also, the median  $J - K$  color as inferred from the photometry is  $\sim 0.1$  mag too blue, while the median  $R - K$  is  $\sim 0.15$  mag too red. This may reflect the fact that dusty galaxies (see § 3.4) with relatively red  $R - K$  and blue  $J - K$  colors fall out of the sample, and move to lower redshift. Nonetheless, the photometric and spectroscopic distributions are remarkably similar for both  $J - K$  and  $R - K$ .

The systematics in both the photometric mass and redshift distribution introduce a systematic in number of massive galaxies in a certain redshift interval, as shown in Figure 16. As both the photometric masses and redshifts at  $z \sim 2.5$  are generally overestimated, the number of massive galaxies and the mass density will be lower than inferred from the photometry. Our sample is too small to directly quantify this effect. However, we can use the originally photometric sample to estimate the change of the number of massive galaxies in certain redshift bins.

We construct a  $K$ -selected ( $K < 21.3$ ) photometric galaxy sample from the deep MUSYC catalog, and correct this sample using the coupled distributions of  $(z_{\text{phot}} - z_{\text{spec}})/(1 + z_{\text{spec}})$  and  $M_{\text{spec}}/M_{\text{phot}}$ . For these distributions we solely use the GNIRS galaxies in the deep fields (excluding ECDFS galaxies). As galaxies will scatter in and out of the relevant redshift interval ( $2 < z < 3$ ) from both low and high redshift, we start with a photometric sample over a larger redshift interval ( $1.5 < z < 4.0$ ). We randomly apply the coupled distributions to the original sample, and repeat this process 1000 times. From the original sample and all 1000 simulations we construct a mass-limited sample ( $> 10^{11} M_{\odot}$ ). We apply the mass-cut after correcting, as galaxies that do not make the cut in the original sample can still scatter into the corrected sample. The depth of the  $K$ -selected catalog allows extraction of an almost complete mass-limited sample (van Dokkum et al. 2006). Finally, we divide the sample in redshift bins of  $\Delta z = 0.1$  and average the simulation to construct the final corrected number distribution. Figure 17 presents both the original and corrected number distributions of a mass-limited sample as a function of redshift.

The difference in the original and corrected distribution in Figure 17 shows that photometric studies may overestimate the number of massive galaxies by a factor of  $\sim 1.3$  at  $2 < z < 3$ . However, this test is a simplification. First, we used the same coupled distributions of  $(z_{\text{phot}} - z_{\text{spec}})/(1 + z_{\text{spec}})$  and  $M_{\text{spec}}/M_{\text{phot}}$  randomly for all galaxies, while we know that there are correlations between  $\Delta z/(1 + z)$  and S/N of the photometry,  $K$  magnitude, SED type etc. (see § 3.4). Our spectroscopic sample is too small to quantify these correlations in an applicable form. Second, our sample and thus the

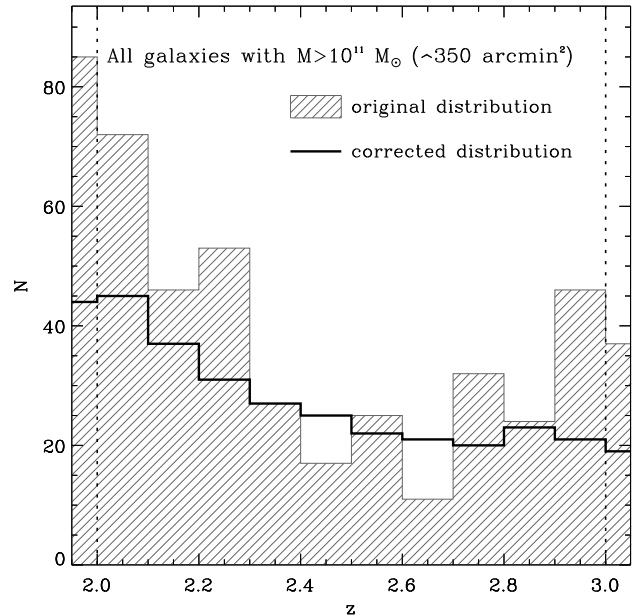


FIG. 17.— The original and corrected number of galaxies with  $M > 10^{11} M_{\odot}$  vs. redshift in the deep MUSYC fields. The original distribution is based on  $z_{\text{phot}}$  and photometric masses. The corrected distribution is estimated using the coupled distributions of  $(z_{\text{phot}} - z_{\text{spec}})/(1 + z_{\text{spec}})$  and  $M_{\text{spec}}/M_{\text{phot}}$ , as explained in the text. This figure illustrates that the number of massive galaxies with  $M > 10^{11} M_{\odot}$  in the range  $2 < z < 3$  is likely lower than previously derived by van Dokkum et al. (2006) using only photometric information.

distributions of  $\Delta z/(1 + z)$  and  $M_{\text{spec}}/M_{\text{phot}}$  may be incomplete. For example, it may be that we miss galaxies with a  $z_{\text{phot}} \sim 4$  and a  $z_{\text{spec}} \sim 2$ . A larger sample over a larger redshift range is needed to better understand the systematics.

#### 4.3. Implications for Previous Studies

At this moment most studies of massive galaxies beyond  $z > 1.5$  rely on photometric redshifts. Thus, the systematics found in this work will have consequences for previous studies, especially to those that use the same or a similar method to derive photometric redshifts. In this section we will discuss several studies and how our findings may affect their results.

Using a photometric mass-limited sample ( $M > 10^{11} M_{\odot}$ ) van Dokkum et al. (2006) recently showed that massive galaxies at  $2 < z < 3$  have red rest-frame optical colors, and found a median  $J - K$  and rest-frame  $U - V$  color of 2.48 and 0.62 respectively. This study also contained the deep MUSYC fields (in addition to several other deep fields) and used the same photometric redshift code as used in this paper. In the previous section we showed that the distributions of  $J - K$  and  $R - K$  barely changes when including the spectroscopic information. The rest-frame  $U - V$  color is slightly redder and more peaked, but this difference is consistent with the photometric errors. Thus, our spectroscopic study does not change, but supports the overall conclusion by van Dokkum et al. (2006) that the high mass end at  $2 < z < 3$  is dominated by red galaxies.

Although the colors of massive galaxies at  $2 < z < 3$  barely change when including spectroscopic information, the number of massive galaxies decreases (see § 4.2). This

will be of importance for our understanding of the evolution of the mass density (e.g., Dickinson et al. 2003; Rudnick et al. 2003, 2006; Drory et al. 2005). Due to the numerous low redshift spectroscopic surveys, photometric redshifts below  $z = 1$  are well calibrated and have small uncertainties in the order of  $\Delta z/(1+z) \sim 0.03$ . This results in well-calibrated masses. However, as shown in this paper, photometric redshifts beyond  $z > 1.5$  are generally poorly calibrated and may show strong systematics. These systematics may result in too high redshifts, and thus too high stellar masses. For the photometric redshift code and template set used in this paper, the evolution of the global stellar mass density between  $z \sim 2.5$  and  $z \sim 0$  would have been underestimated by a factor of  $\sim 1.3$ , due to the combination of redshift and mass systematics. However, this factor is almost entirely driven by overestimates of photometric redshifts. As other studies may use different  $z_{\text{phot}}$  codes and templates sets, they may not suffer from this effect.

Our results will also affect galaxy clustering studies (e.g., Daddi et al. 2003; Quadri et al. 2007a; Foucaud et al. 2007). Galaxy clustering at high redshift is measured using the angular two-point correlation function. The angular correlation function can be converted into the spatial correlation function using the Limber equation. The main ingredient in this equation is the redshift distribution. Quadri et al. (2007a) use the summed redshift probability distribution, in order to account for different  $z_{\text{phot}}$  errors of the individual galaxies. In the two bottom panels of Figure 10 we compare the summed probability distributions of the photometric redshifts of the GNIRS galaxies for both the full and deep sample, with the spectroscopic distribution. For the continuum redshifts we use the probability distribution as well. Although the median of the distribution for both samples is slightly offset in redshift, the width of the distribution is similar. Because the Limber deprojection is more dependent on changes to the width of the distribution than the central value, the clustering results will not change significantly when using spectroscopic redshifts. One can argue that this might be coincidence and further study is necessary to confirm this.

## 5. SUMMARY

In this paper we present our complete NIR spectroscopic survey for  $K$ -selected galaxies at  $z \sim 2.3$ . We acquired high quality NIR spectra ( $1.2\text{--}2.5 \mu\text{m}$ ) with GNIRS for a total sample of 36 galaxies. The galaxies were selected to be bright in  $K$  ( $< 19.7$ ) and have photometric redshifts in the range  $2.0 \lesssim z \lesssim 3.0$ . All galaxies have photometric stellar masses  $> 10^{11} M_{\odot}$ . The distribution of observed  $J - K$ ,  $R - K$  and photometric rest-frame  $U - V$  colors are similar as those of a photometric mass-limited sample extracted from the deep MUSYC fields. This suggests that our spectroscopic sample is representative for a mass-limited ( $> 10^{11} M_{\odot}$ ) sample at  $2 < z_{\text{phot}} < 3$ . Our sample is not representative for a  $K$ -bright galaxy sample, as our redshift distribution is slightly higher. Nevertheless, the distribution of photometric rest-frame  $U - V$  colors is similar for the GNIRS sample and the full  $K$ -bright photometric sample.

We successfully derived spectroscopic redshifts for all galaxies. For 19 of the galaxies we detected rest-frame

optical emission lines, which provided us with accurate redshift measurements. For the remaining galaxies we derived redshifts by modeling the continuum spectra in combination with the optical photometry. We tested this method using the emission-line galaxies, and found a scatter of  $\Delta z/(1+z) = 0.019$ , and no significant systematic offset. The continuum redshifts are more accurate for optically red galaxies, with large Balmer/4000 Å breaks, and for redshifts for which the break falls in an atmospheric window.

Comparison with spectroscopic redshifts shows that the original photometric redshifts are generally overestimated by  $\Delta z/(1+z) = 0.08$ , and have a scatter of  $\Delta z/(1+z) = 0.13$ . Both the systematic and the scatter are worse for galaxies with shallow NIR photometry ( $K \sim 20$ ). For the galaxies with deeper NIR photometry ( $K \sim 21$ ) we find a systematic offset of  $\Delta z/(1+z) = 0.03$  and a scatter of  $\Delta z/(1+z) = 0.08$ .

In addition to shallow NIR photometry, the lack of well calibrated galaxy templates is another important cause for the large systematics and scatter of photometric redshifts. Especially, dusty and/or young galaxies have high  $\Delta z/(1+z)$ . This may not be surprising as the original template set of our photometric redshift code lacked these galaxies. We almost completely remove the systematic offset when repeating the fitting procedure replacing the original templates by 6 SEDs chosen from fits to the spectroscopic sample. We examine other possible causes for the scatter and systematics in  $\Delta z/(1+z)$  as well. Emission line contamination is only of minor importance for this sample and may affect the  $z_{\text{phot}}$  for some individual galaxies. Furthermore, we find a correlation with  $K$ -band magnitude, such that  $K$ -bright galaxies in general have larger  $\Delta z/(1+z)$  than those faint in  $K$ . This effect may be diminished by using a luminosity prior in the photometric redshift code. Although improved photometric redshift codes and better templates may remove the systematics and decrease the scatter, photometric redshifts remain limited by the low resolution spectral shape, and are not likely to surpass a scatter of  $\Delta z/(1+z) = 0.05$  at the targeted redshift range – even for the galaxies with deep NIR photometry. We note that obtaining photometry in narrower bands and for a larger number of filters may lead to better results than has typically been the case to date.

The spectroscopic stellar population properties, as derived by modeling the spectral continuum shape together with optical photometry, allow us to examine the significance and reliability of the stellar population properties derived from the photometry alone. Strikingly, the properties age, SFR,  $\tau$  show a scatter of a factor of  $\sim 3 - 4$  between the photometrically and spectroscopically derived properties. For  $A_V$  this scatter is  $\sim 1$  mag. The improvement in age and  $\tau$  is driven primarily by the higher resolution spectral shape, and less so by the better constrained redshift. For SFR and  $A_V$  both effects are about equally important. The uncertainties in the photometric modeling seem reasonable, as for  $\sim 3/4$  of the galaxies the photometric and spectroscopic properties are consistent within  $1\sigma$ . Nevertheless, the photometric and spectroscopic distributions are quite different, accounting for their errors. This may be caused by the fact that age,  $A_V$  and  $\tau$  suffer from systematics, due to degeneracies with the photometric redshift. For example, the photometric

stellar population properties for several galaxies converge to the properties of best-fit templates, used in the photometric redshift code. This all implies that the best-fit photometric properties and especially their distribution are strongly biased.

The photometrically derived stellar mass and mass-to-light ( $M/L_V$ ) ratio are best determined and show a scatter of a factor of  $\sim 2$  with their spectroscopic analogues. However, the systematic offset in  $\Delta z/(1+z)$  results in a systematic offset in  $M_{\text{phot}}/M_{\text{spec}}$ , such that  $M_{\text{phot}}$  is about 30% too high for the galaxies with deep NIR photometry. This systematic is canceled out in  $M/L_V$ , as the  $L_{V,\text{phot}}$  suffers from similar systematics as  $M_{\text{phot}}$ . The improvement for both stellar mass and  $M/L_V$  is about equally driven by the higher resolution spectral shape and the better constrained redshift.

Rest-frame  $V$  magnitudes and  $U - V$  colors are the derived properties which are most sensitive to photometric redshift uncertainties and low S/N photometry. The scatter between the photometrically and spectroscopically derived properties is 0.4 and 0.2 mag for  $V$  and  $U - V$  respectively for galaxies with deep NIR photometry, and both increase by 50% when we include the galaxies with shallow photometry. The systematics in the photometric redshifts cause a systematic offset of -0.2 and -0.1 mag for  $V$  and  $U - V$  for galaxies with deep NIR photometry. Thus, for both the scatter and the systematics, the improvement is almost completely driven by better constrained redshifts.

In order to assess the impact of the identified systematics on complete photometric samples, we compared photometric and spectroscopic samples in the same mass and redshift range. Surprisingly, we found that the distribution of  $J - K$  and  $R - K$  color barely changes for massive galaxies ( $> 10^{11} M_{\odot}$ ) at  $2.0 < z < 2.7$ . Thus, the

spectroscopy supports previous studies that red galaxies dominate the high mass end at  $z \sim 2.5$ . However, the combination of photometric redshift and stellar mass systematics also affect the number of massive galaxies. The photometric redshift code and template set used in this work overestimates the number of massive galaxies by factor of  $\sim 1.3$  at  $2 < z < 3$ , resulting in an underestimation of the stellar mass density between  $z \sim 2$  and  $z \sim 0$ .

Overall, our spectroscopic survey demonstrates the large uncertainties of best-fit photometric properties, and the necessity for accurate calibration of photometric studies. Although this study is a step forward in understanding the systematics in photometric studies of massive galaxies at  $z > 2$ , larger spectroscopic samples over a larger redshift range are needed to fully map the systematics and accurately calibrate photometric studies. Furthermore, this study only applies to the high-mass end of the high-redshift galaxy population. Less massive galaxies may have other systematics, although that remains to be explored.

We thank Gemini Observatory for their enthusiasm and support of our program. We also thank the anonymous referee for valuable comments on the manuscript. This research was supported by grants from the Netherlands Foundation for Research (NWO), the Leids Kerkhoven-Bosscha Fonds, National Science Foundation grant NSF CAREER AST-044967, and NASA LTSA NNG04GE12G. DM is supported by NASA LTSA NNG04GE12G. EG is supported by an NSF Astronomy & Astrophysics Postdoctoral Fellowships under award AST-0401547. PL acknowledges support from Fondecyt Grant no. 1040719.

## REFERENCES

- Beers, T. C., Flynn, K., Gebhardt, K. 1990, *AJ*, 100, 32  
 Bruzual, G. & Charlot, S. 2003, *MNRAS*, 344, 1000  
 Calzetti, D., Armus, L., Bohlin, R. C., Kinney, A. L., Koornheef, J., & Storchi-Bergmann, T. 2000, *ApJ*, 533, 682  
 Coleman, G. D., Wu, C.-C., & Weedman, D. W. 1980, *ApJS*, 43, 393  
 Chabrier, G. 2003, *PASP*, 115, 763  
 Dahlen, T., Mobasher, B., Somerville, R. S., Moustakas, L. A., Dickinson, M., Ferguson, H. C., & Giavalisco, M. 2005, *ApJ*, 631, 126  
 Daddi, E., et al. 2003, *ApJ*, 588, 50  
 Daddi, E., et al. 2004, *ApJ*, 617, 746  
 Daddi, E., et al. 2005, *ApJ*, 600, L127  
 Dickinson, M., Papovich, C., Ferguson, H. C., & Budavári, T. 2003, *ApJ*, 587, 25  
 Drory, N., Salvato, M., Gabasch, A., Bender, R., Hopp, U., Feulner, G., & Pannella, M. 2005, *ApJ*, 619, L131  
 Elias, J.H., et al. 2006, *SPiE* 6269, 139  
 Foucaud, S., et al. 2007, *MNRAS*, 376, L20  
 Förster Schreiber, N. M., et al. 2004, *ApJ*, 616, 40  
 Franx, M., et al. 2003, *ApJ*, 587, L79  
 Gawiser, E. et al. 2006, *ApJS*, 162, 1  
 Giavalisco, M. et al. 2004 *ApJ*, 600, L93  
 Kannappan, S.J., & Gawiser, E. 2007, *ApJ*, 657, L5  
 Kinney, A. L., et al. 1996, *ApJ*, 467, 38  
 Kriek, M., et al. 2006a, *ApJ*, 645, 44  
 Kriek, M., et al. 2006b, *ApJ*, 649, L71  
 Kriek, M., et al. 2007, *ApJ*, 669, 776  
 Kroupa, P. 2001, *MNRAS*, 322, 231  
 Labbé, I., et al. 2005, *ApJ*, 624, L81  
 Maraston, C. 2005, *MNRAS*, 362, 799  
 Marchesini, D., et al. 2007, *ApJ*, 656, 42  
 Papovich, C., Dickinson, M., & Ferguson, H. C. 2001, *ApJ*, 559, 620  
 Papovich, C., et al. 2006, *ApJ*, 640, 92  
 Quadri, R., et al. 2007, *ApJ*, 654, 138  
 Quadri, R., et al. 2007, *AJ*, 134, 1103  
 Rudnick, G., et al. 2001, *AJ*, 122, 2205  
 Rudnick, G., et al. 2003, *ApJ*, 599, 847  
 Rudnick, G., et al. 2006, *ApJ*, 650, 624  
 Salpeter, E.E. 1955, *ApJ*, 121, 161  
 Saracco, P., et al. 2006, *MNRAS*, 367, 349  
 Shapley, A. E., Steidel, C. C., Erb, D. K., Reddy, N. A., Adelberger, K. L., Pettini, M., Barmby, P., & Huang, J. 2005, *ApJ*, 626, 698  
 Steidel, C. C., Giavalisco, M., Dickinson, M., & Adelberger, K.L. 1996a, *AJ*, 112, 352  
 Steidel, C. C., Giavalisco, M., Pettini, M., Dickinson, M., & Adelberger, K.L., 1996b, *ApJ*, 462, L17  
 Steidel, C. C., Adelberger, K. L., Shapley, A. E., Pettini, M., Dickinson, M., & Giavalisco, M. 2003, *ApJ*, 592, 728  
 van Dokkum, P. G., et al. 2003, *ApJ*, 587, L83  
 van Dokkum, P. G., Kriek, M., Rodgers, B., Franx, M., & Puxley, P. 2005, *ApJ*, 622, L13  
 van Dokkum, P. G., et al. 2006, *ApJ*, 638, L59  
 Wuyts, S., et al. 2007, *ApJ*, 656, 42  
 Wuyts, S., et al. 2008, *ApJ*, to be submitted